

1 Water flow timing, quantity, and sources in a fractured high mountain 2 permafrost rock wall

3 Matan Ben-Asher¹, Antoine Chabas², Jean-Yves Josnin², Josué Bock², Emmanuel Malet², Amaël
4 Poulain³, Yves Perrette², Florence Magnin²

5 ¹ Department of Natural Sciences, Open University of Israel, Ra'anana, Israel

6 ² EDYTEM, USMB, CNRS, 5 bd de la mer Caspienne, 73376 Le Bourget du Lac cedex, France

7 ³ TRAQUA S.A., Namur, Belgium

9 *Correspondence to:* Matan Ben-Asher (matanbe@openu.ac.il) and Florence Magnin (Florence.Magnin@univ-smb.fr)

10 Abstract

11 Water flow in high mountain rock walls is crucial for landscape evolution and slope stability. However, the timing, quantity,
12 and sources of this flow remain poorly understood. In the Mont Blanc massif, tunnels at the Aiguille du Midi peak (3842 m)
13 provide direct access to steep permafrost-affected rock walls. Between May 2022 and October 2023, we monitored water
14 flowing from fractures using a real-time system that measured flow rate, temperature, electrical conductivity, and fluorescence
15 of tracers, alongside meteorological data and ground surface temperatures.

16 The results indicate high surface–subsurface connectivity. The water source is primarily snowmelt, with additional inputs from
17 late-summer rainfall. Electrical conductivity, stable isotopes, and recession curve analysis suggest another source of older
18 subsurface ice. Flow onset was closely tied to air temperatures, with steady diurnal fluctuations appearing once rock surface
19 temperatures exceeded 0 °C. Lag times between daily peaks of flow rate and peaks of air and ground surface temperatures of
20 3–9 hours and 0–3 hours, respectively, point to rapid unsaturated infiltration conditions. Distinct flow regimes observed in two
21 adjacent fracture systems reflect a complex, heterogeneous network, including sediment-filled fractures with a delayed
22 response. Significant flow rates (often >10 L/h) and water temperature often exceeding 5 °C, suggest significant heat transfer
23 by advection, capable of enhancing permafrost degradation.

24 This study provides rare direct observations of fracture flow dynamics in steep permafrost rocks, and improves our
25 understanding of water routing and its response to atmospheric forcing. The findings offer valuable constraints for coupled
26 hydrothermal models, permafrost-related hazard assessments, and the potential impact of climate change.

27
28 **Key words:** Permafrost, monitoring, water infiltration, Mont Blanc massif, climate change

Style Definition: Heading 1: Outline numbered + Level: 1 +
Numbering Style: 1, 2, 3, ... + Start at: 1 + Alignment: Left +
Aligned at: 0 cm + Tab after: 0 cm + Indent at: 0.63 cm

Style Definition: Bullets: Outline numbered + Level: 1 +
Numbering Style: 1, 2, 3, ... + Start at: 1 + Alignment: Right
+ Aligned at: 0.63 cm + Tab after: 0 cm + Indent at: 1.27

Style Definition: MS title

Style Definition: List Paragraph

Style Definition: Affiliation

Style Definition: Authors

Style Definition: Comment Text

Style Definition: equations cupernicus: Indent: Before: 0
cm, Hanging: 2 cm, Outline numbered + Level: 1 +
Numbering Style: 1, 2, 3, ... + Start at: 1 + Alignment: Left +
Aligned at: 0 cm + Tab after: 1.27 cm + Indent at: 1.27 cm

Style Definition: math symbol

Style Definition: Comment Subject

Style Definition: Revision

Style Definition: Bibliography

29 1. Introduction

30 1.1. Hydrogeology of high mountains

31 Water plays a crucial role in weathering and erosion processes in mountainous landscapes. In the periglacial belt, the presence
32 of water in the shallow subsurface can cause rock fracturing through ice segregation or volumetric expansion, depending on
33 temperature conditions and saturation levels ([Dracbing and Krautblatter, 2019](#); [Matsuoka and Murton, 2008](#)); ([Dracbing and](#)
34 [Krautblatter, 2019](#); [Matsuoka and Murton, 2008](#)). Hydrostatic pressure in undrained fractures can drive catastrophic failure
35 ([Hasler et al., 2012](#); [Krautblatter et al., 2013](#); [Scandroglio et al., 2021](#); [Walter et al., 2020](#)); ([Hasler et al., 2012](#); [Krautblatter et](#)
36 [al., 2013](#); [Scandroglio et al., 2021](#); [Walter et al., 2020](#)). Over geological time scales water is a key catalyst of mechanical rock
37 weathering processes related to subcritical cracking ([Eppes and Keanini, 2017](#)); ([Eppes and Keanini, 2017](#)). The melting of ice
38 in joints under thawing conditions can release detached blocks and lead to debris and rock falls, and the formation of scree
39 slopes ([Hales and Roering, 2007](#)); ([Hales and Roering, 2007](#)). Water infiltration in bedrock may also trigger large rock slope
40 failures by reducing the friction of rough fracture contact surfaces ([Krautblatter et al., 2013](#)); ([Krautblatter et al., 2013](#)). In
41 permafrost ground, the presence of sealing ice in pores and fractures favors the development of high hydrostatic pressures
42 ([Fischer et al., 2010](#); [Marcer et al., 2020](#)), which may increase the frequency or magnitude of mass movements. In addition to
43 mechanical pressure, water circulation can also cause thermal perturbations with potential cooling effects in some cases
44 ([Maréchal et al., 1999](#); [Phillips et al., 2016](#)) or warming effects in others ([Hasler et al., 2011](#); [Phillips et al., 2016](#)); ([Maréchal](#)
45 [et al., 1999](#); [Phillips et al., 2016](#)) or warming effects in others ([Hasler et al., 2011](#); [Phillips et al., 2016](#)). In permafrost ground,
46 heat advection from water infiltration could accelerate permafrost degradation ([Gruber and Haeberli, 2007](#); [Hasler et al., 2011](#);
47 [Magnin and Josnin, 2021](#)); ([Gruber and Haeberli, 2007](#); [Hasler et al., 2011](#); [Magnin and Josnin, 2021](#)), and potentially develop
48 thawing corridors ([Krautblatter and Hauck, 2007](#); [Keusing et al., 2017](#)). Recent observations of increased rock fall activity in
49 high mountains regions have been linked to permafrost degradation ([Allen et al., 2009](#); [Fey et al., 2025](#); [Gruber et al., 2004](#);
50 [Huggel et al., 2012](#); [Legay et al., 2021](#); [Raveland et al., 2017](#); [Raveland and Deline, 2011](#)); ([Allen et al., 2009](#); [Fey et al., 2025](#);
51 [Gruber et al., 2004](#); [Huggel et al., 2012](#); [Legay et al., 2021](#); [Raveland et al., 2017](#); [Raveland and Deline, 2011](#)). The warming of
52 intact frozen rock is commonly related to rockwall destabilization due to a decrease in rock uniaxial and tensile strength
53 ([Dwivedi et al., 1998](#); [Krautblatter et al., 2013](#); [Li et al., 2003](#); [Mellor, 1973](#)); ([Dwivedi et al., 1998](#); [Krautblatter et al., 2013](#);
54 [Li et al., 2003](#); [Mellor, 1973](#)). Water-related processes have been suggested as a potential cause of several rock fall events
55 ([Cathala et al., 2024](#); [Erismann and Abele, 2001](#); [Scandroglio et al., 2021](#); [Strauhal et al., 2016](#)). However, while
56 hydrogeological studies in alpine permafrost have primarily focused on coarse-grained terrain, such as rock glaciers ([Bast et](#)
57 [al., 2024](#)) and scree slopes ([Pellet and Hauck, 2017](#)); ([Bast et al., 2024](#)) and scree slopes ([Pellet and Hauck, 2017](#)), little is known
58 about water dynamics within bedrock rockwalls—despite their critical role in slope stability and landscape evolution.

59 1.2. Existing knowledge on water flow and infiltration in mountain permafrost

60 In steep alpine bedrock, the question of water infiltration and its thermal and mechanical implications is crucial but is rarely
61 addressed directly (~~Krautblatter et al., 2013~~)(Krautblatter et al., 2013). Studying hydrogeological processes in these
62 environments poses several challenges, including limited accessibility, the hidden nature of water flow pathways, strong spatial
63 and temporal variability, non-linear system behavior, and the difficulty of identifying water sources quantitatively. Hasler et
64 al. (2011) used numerical simulations to explore the impact of advective heat transport by water percolation on subsurface
65 temperatures and ice-level changes.(2011) used numerical simulations to explore the impact of advective heat transport by
66 water percolation on subsurface temperatures and ice-level changes. In the absence of hydrogeological field measurements,
67 they performed laboratory experiments and demonstrated significant implications for the role of water flow in thaw-related
68 instabilities in cold mountain permafrost regions. Maréchal et al. (1999) used a hydrothermal model to simulate an observed
69 thermal anomaly that was found during drilling work in the road tunnel under the Mont-Blanc massif and showed that
70 infiltration of water from the surface contributed to the continuous cooling of the alpine massif at depth. Ben-Asher et al.
71 (2023) estimated the potential water input in steep alpine bedrock using field measurements and numerical simulations.
72 Apart from indirect studies (~~Ben-Asher et al., 2023; Hasler et al., 2011; Maréchal et al., 1999; Seherler et al., 2010~~)(Ben-Asher
73 et al., 2023; Hasler et al., 2011; Maréchal et al., 1999; Scherler et al., 2010), few studies have attempted to directly monitor
74 groundwater flow in steep, permafrost-affected alpine environments (~~Gabrielli et al., 2012; Manning and Caine,
75 2007~~)(Gabrielli et al., 2012; Manning and Caine, 2007). In a recent study, Scandroglia et al. (2025) measured water outflow
76 in 55 m deep fractures under the permafrost-affected Zugspitze Ridge (2815–2962 m a.s.l). They compared their dataset with
77 meteorological data and a snowmelt model to infer the timing and quantity of water flow and constrain the hydrological
78 pressure in the fractures. They also analyzed recession curves of the measured flow rate, a technique that was never applied to
79 alpine rock fractures before.

80 1.3. Saturated and non-saturated flow

81 From a hydrogeological perspective, a fractured summit is more accurately described as a permeable infiltration zone than as
82 an aquifer. However, due to the scarcity of drilling data, constraints on the thickness of the high-elevation alpine unsaturated
83 zone remain highly limited (Maréchal, 1998). The first tests of hydrodynamical models of a high alpine and permafrost-
84 affected rock wall site were performed by Magnin & Josnin (2021) on the Aiguille du Midi site. This study showed that the
85 unsaturated zone is probably more than 1000 m thick. In the Rocky Mountains, several hundred meters of unsaturated zone
86 above the water table have also been reported (Russell et al. 2001).

87 Generally, unsaturated conditions apply in soils, permeable rocks, and deposits, and water flow is often considered subvertical
88 and evaluated using the Richards equation (Smith, 2002). In crystalline rock settings, porosity and permeability are essentially
89 controlled by the geometry of the fracture network, where most of the water flow occurs. The water flow in fractures is thus
90 not uniform but occurs along preferential flow paths sometimes called “fingers” (Su et al., 2000), that channel the flow path

91 at the larger scale of the fractured medium (Tsang et al., 2013). These preferential flow paths have been observed in both
92 saturated and unsaturated fractures (Su et al., 2000).

93 In the study area of the Mont-Blanc massif, the fracture network opening is highly irregular (from millimeters to decimeters,
94 depending on the fractures) and is expected to evolve seasonally, with reversible opening in winter (Guillet et al., 2018)(Guillet
95 et al., 2018), superimposed on an irreversible long-term opening trend (Weber et al., 2017). The fractures can also be affected
96 by the water flow, which can change the extent of ice filling or plugging and develop partially saturated conditions similar to
97 those known from some epikarsts (Ford and Williams, 1989)(Ford and Williams, 1989).

98 ~~This study is motivated by the need to better understand hydrological processes in high mountain permafrost environments~~
99 ~~and connectivity with changing surface conditions, particularly in the context~~The objective of ongoing climate change. We
100 ~~aim to address major knowledge gaps in the hydrology of high elevation permafrost rock regarding~~this work is to quantify the
101 ~~timing, quantity, and sources~~sources of water flow in the fractures, and within this fractured permafrost rock wall, and to
102 ~~evaluate how the flow is affected by surface~~dynamics are influenced by atmospheric forcing and surface conditions.
103 Specifically, we aim to (1) characterize seasonal and diurnal variability in fracture flow, (2) assess the relative contribution of
104 different water sources, and (3) examine the coupling between thermal conditions and hydrological response.
105 In the next sections, we first introduce the study area and monitoring approach and then describe the data and analytical
106 methods. We then present the source~~main~~hydrological and thermal observations and examine their implications for water
107 flow processes in fractured permafrost rock walls. The paper concludes with a synthesis of infiltrating water. The key findings
108 and their broader significance.

109 2. Study site and meteorological context

110 1.4.2.1. Aiguille du Midi site

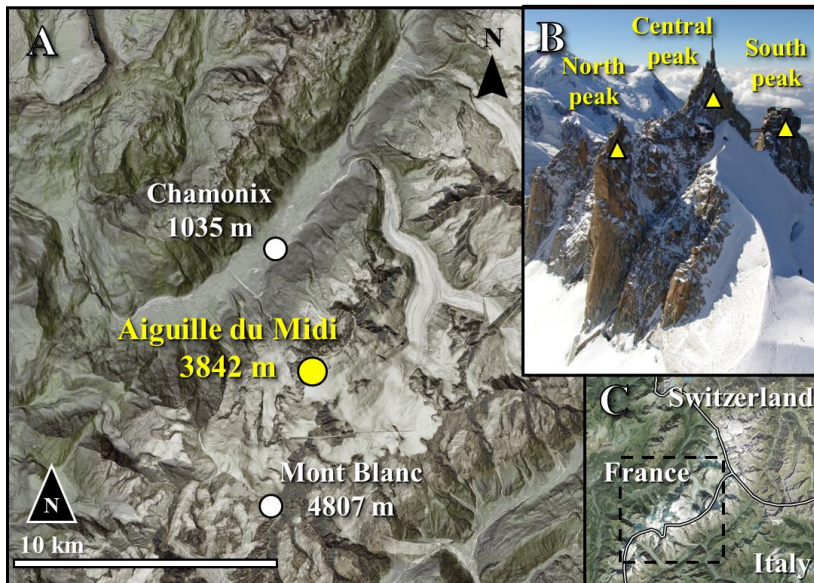
111 The Aiguille du Midi (AdM) is a peak composed of three granite pillars - Piton Nord, Piton Central, and Piton Sud. The central
112 pillar (Piton Central) reaches an elevation of 3842 m a.s.l and towers approximately 3000 m above the valley of Chamonix
113 (Figure 1). **Figure 1**). The site lies on the NW flank of the Mont Blanc massif (MBM) which covers an area of about 550 km²
114 and is oriented NW-SE between France, Italy, and Switzerland.

115 Glaciers occupied about 100 km² in the late 2000s (Gardent et al., 2014)(Gardent et al., 2014) while permafrost is largely
116 present above approximately 2600 m in N faces and 3200 m in S faces (Magnin et al., 2015a).

117 The combination of steepness, permafrost, and glacial dynamics results in highly active morphodynamics (Deline et al., 2015).
118 Over the past decades, rockfall (volume > 100 m³) frequency has significantly increased (Raveland and Deline, 2011), notably
119 during the hot summers. The main cause has been suggested to be permafrost degradation (Raveland et al., 2017; Legay et al.,
120 2021; Magnin et al., 2023). Permafrost investigation started in the mid-2000s in the MBM, with the installation of various

121 temperature sensors in AdM (Magnin et al., 2015b)(Magnin et al., 2015b), including 10-m deep boreholes, which recorded a
122 temperature increase of over 1 °C during the 2011-2020 decade (Magnin et al., 2024).

123 AdM has been chosen as a pilot site for alpine permafrost investigations because of its representativeness of high alpine
124 rockwalls and its accessibility from Chamonix by a cable-car. Man-made tunnels, terraces, bridges, and an elevator allow the
125 visitors to access different parts of the site. Since the hot summer of 2015, water flowing from the fractured tunnel walls has
126 become a problem for the operating company (the *Compagnie du Mont Blanc*), leading to the installation of a drained metal
127 plate ceiling to divert the flowing water and keep some parts of the tunnels dry for visitors.

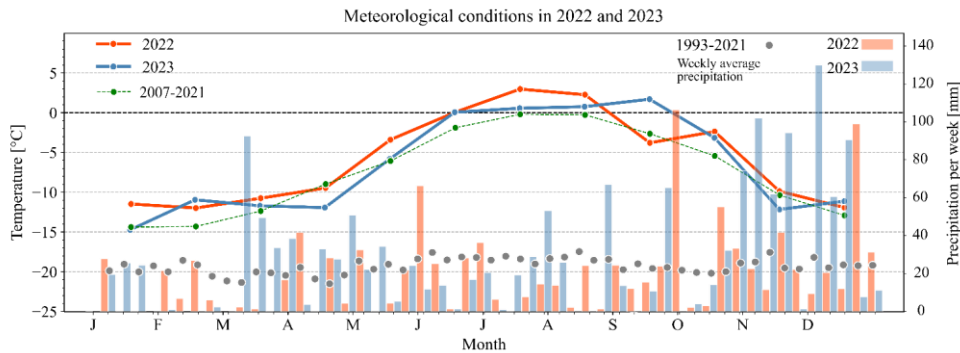


128
129 **Figure 1:** A) Location of the Aiguille du Midi in the Mont Blanc massif. B) view of the three peaks at Aiguille du Midi. (Picture: S.
130 Gruber). C) Location of the Mont Blanc massif on the border of France, Italy and Switzerland. Maps provided by the Swiss Federal
131 Office of Topography swisstopo.

132 1.5.2.2. Meteorological conditions in 2022 and 2023

133 As of 2024, in Europe, the years 2022 and 2023 were the third and second warmest years in record after 2020, respectively,
134 with a mean annual air temperature (MAAT) about 1.1 °C above the 1991-2020 average (ESOTC 2023, 2024). Summer 2022

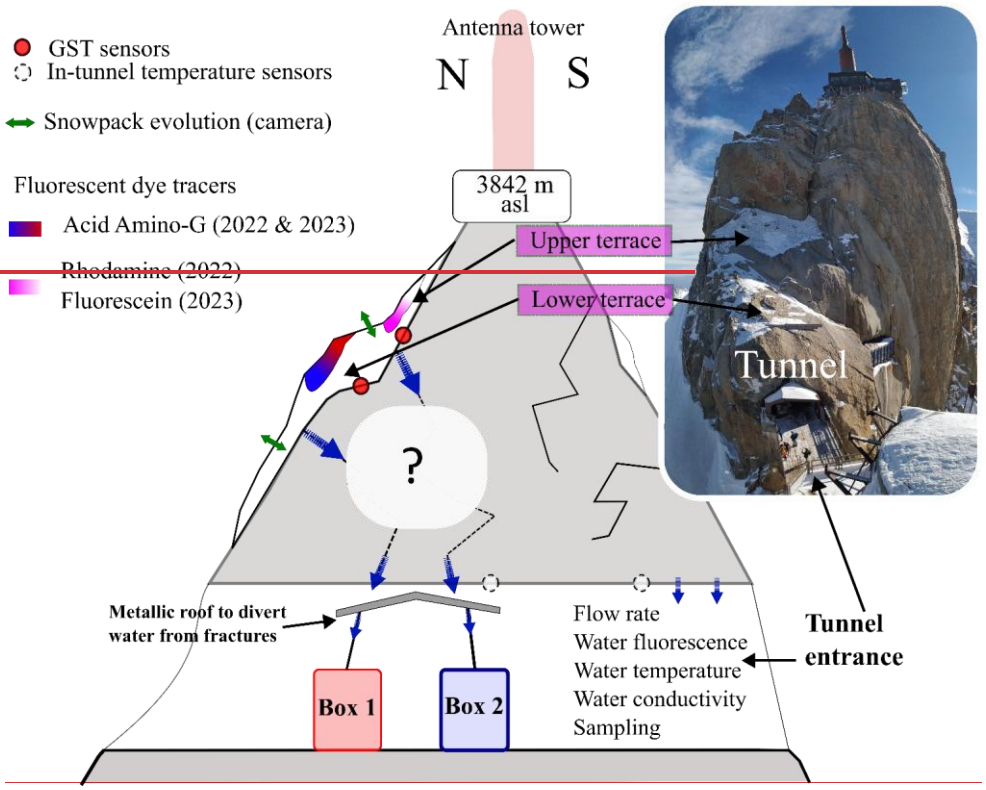
135 was the warmest summer ever recorded, outpacing the 1991-2020 average by 1.4°C (ESOTC, 2023). September 2023 was the
 136 warmest September on record (EOSTC, 2023).
 137 Air temperature (AT) and precipitation records in the town of Chamonix (France), located in the valley just north of AdM
 138 (Fig. 1), began in the early 20th century and are well-suited to characterize the local precipitation regime. At AdM, AT records
 139 started in 2007 but are affected by numerous gaps that sometimes last several months, making this data less reliable for multi-
 140 annual comparison.
 141 Figure 2 shows AT and precipitation in Chamonix and at AdM for 2022–2023 (Figure 2). Winter and early spring 2022 were
 142 markedly warmer and drier than in 2023, with mean AT at AdM about 1.4 °C higher and precipitation roughly half as much.
 143 A late-spring heat wave produced a record high AT in May 2022, while May 2023 was near average. Summer conditions were
 144 generally warmer in 2022, but an exceptional late-season heat wave occurred in September 2023—the warmest on record in
 145 Chamonix—, whereas September 2022 was near normal. Overall, 2023 was wetter than 2022, mainly due to higher
 146 precipitation in spring and autumn.
 147 In summary, 2022 was characterized by a very early but long-lasting and record-breaking summer heat wave, while 2023 was
 148 characterized by a late and record-breaking summer heat wave with significantly more precipitation than in 2022.

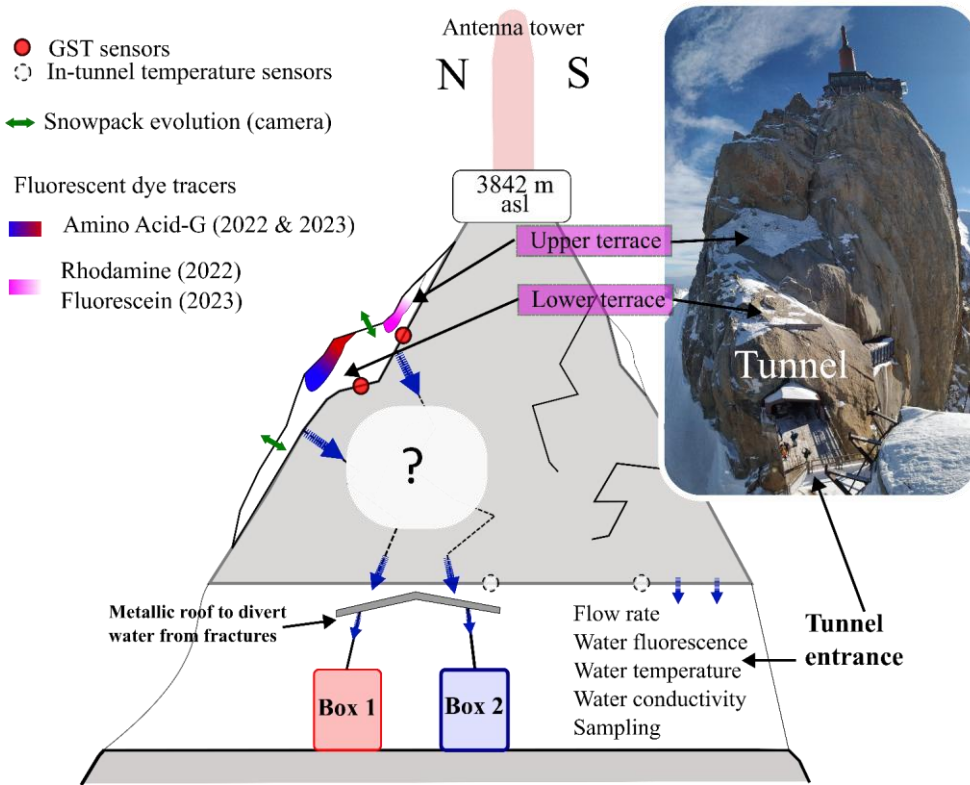


151
 152 **Figure 2: Monthly average air temperatures (Lines) and weekly precipitation (bars) in 2022 (orange) and 2023 (blue). Air**
 153 **temperature was measured at the site in Aiguille du Midi (3842 m a.s.l). Precipitation was measured in Chamonix (1042 m a.s.l),**
 154 **since no reliable precipitation data is available at the high elevation site. Data provided by Météo France. The long-term average**
 155 **air temperature (2007-2021) is presented as a green thin dashed line. The long-term average weekly precipitation in Chamonix**
 156 **(1993-2021) is shown by gray circles.**

157 **3. Methods**

158 In April and May 2022, we installed a monitoring system to measure characteristics of water flowing through fractures in the
159 roof of the tunnel in AdM (Figure 3, Figure 4).





161

162 Figure 3: Sketch of the methodological approach to track and monitor water flows in the Aiguille du Midi central pillar. Note the
 163 location of the insertion of the dye tracers in the snowpacks on the terraces above the water monitoring boxes.

164

4.6.3.1. Fluorescent dyes in the snowpack

165

Fluorescent dyes were inserted into the snowpack at the surface above the tunnel in two locations, directly above the fractures (Figure 3), to trace the water source and rate of infiltration. In the 2022 season, two dye solutions were used: 20 L of sulphorhodamine-B (SRB) solution with a concentration of 0.001 g/L and 20 L of amino acid G (AAG) with a concentration of 20 g/L. These solutions were prepared and carried in "Ondine®" mineral water bottles by inserting the dye powders directly into the original mineral water, each with a volume of 5 L. The relatively low concentration of sulphorhodamine-B SRB was chosen to have a light but detectable pink color, far above the detection limit of the fluorimeter sensor.

170

171 In 2023, new solutions were prepared in the same manner, using 1.5 L bottles of “Ondine®” mineral water. ~~Sulphorhodamine-~~
 172 ~~BSRB~~ was replaced by fluorescein dye, (FLC), a much more soluble and detectable dye, to avoid confusion with
 173 ~~sulphorhodamine-BSRB~~ from the previous year. In total, 9 L of ~~fluoreseeinFLC~~ solution with a concentration of 0.667 g/L
 174 and 16 L of ~~amino-acid-GAAG solution~~ with a concentration of 12.5 g/L were prepared.
 175 In both years of the study, tracers were injected into the snowpack at the same two locations on the north face of the central
 176 peak (Figure 3). ~~Sulphorhodamine-BSRB~~ in 2022 and ~~FluoreseeinFLC~~ in 2023 were injected on the "upper" terrace of the
 177 face, which is located 18-24 meters above the tunnel, while ~~amino-acid-GAAG~~ was injected on the "lower" terrace, 7-12 meters
 178 above the tunnel, in 2022 and 2023. The tracers were inserted in spring, before the flow started: on ~~the~~ 11 May 2022 and 22
 179 March 2023. We poured the solution in 5-10 points on each terrace and on the snowpack surface.

180 4.7.3.2. Ground surface temperature at the snow-rock interface

181 Four miniature temperature sensors (iButtons, Mouser®) have been installed in holes drilled 5 cm into the rock surface, at the
 182 snow-rock interface, on the terraces where the fluorescent dyes were injected. The holes containing the coin-sized sensors
 183 were filled with gray polymer clay to insulate the metal sensors from direct solar radiation. The sensors monitored ground
 184 surface temperature (GST) at hourly time steps and over different periods (Table ~~1~~~~Error! Reference source not found.~~),
 185 but only one (#61B8) monitored the temperatures during both seasons.

Sensor ID	Monitoring period covered	Location on the face
7077	11/05/2022 to 23/09/2022	In drilled hole at base of vertical rock outcrop
6202	06/09/2022 to 22/08/2023	In drilled hole at the surface of the lower terrace
608D	11/05/2022 to 22/08/2023	In a hole drilled at the base of a rock outcrop above the lower terrace
61B8	22/09/2022 to 22/08/2023	In the rock crack (same rock as 608D)

186 **Table 11: Miniature temperature sensors (‘iButtons’) at the snow-rock interface**

187 Snow melting was identified as “zero-curtain” periods in GST (Figure 5). These periods are characterized by stagnant GST at
 188 ~0 °C (~~Hanson and Hoelzle, 2004; Staub and Delaloye, 2017~~).(Hanson and Hoelzle, 2004; Staub and Delaloye, 2017). The
 189 complete melting of the snow is marked by the transition from dampened GST daily oscillations to positive and significant
 190 daily oscillations once the insulating snow layer has melted and solar radiation reaches the rock surface. As GST is measured
 191 at point-scale, it lacks spatial representativeness of the snow melting surface area. Thus, to complete this data, pictures were
 192 frequently taken during fieldwork in 2022 to document snow patch evolution. In 2023, an automatic camera was installed
 193 (Figure 5) on a terrace of the North Pillar (See location on ~~Figure 1~~.)**Figure 1**. From 1 March 2023 to 22 August 2023, it took
 194 4 pictures a day of the north face of the Central Pillar, to monitor the snow patch evolution right above the water collection
 195 system. Pictures after 22 August 2023 are not usable because the protective glass was broken, and the pictures became blurred.

Formatted Table

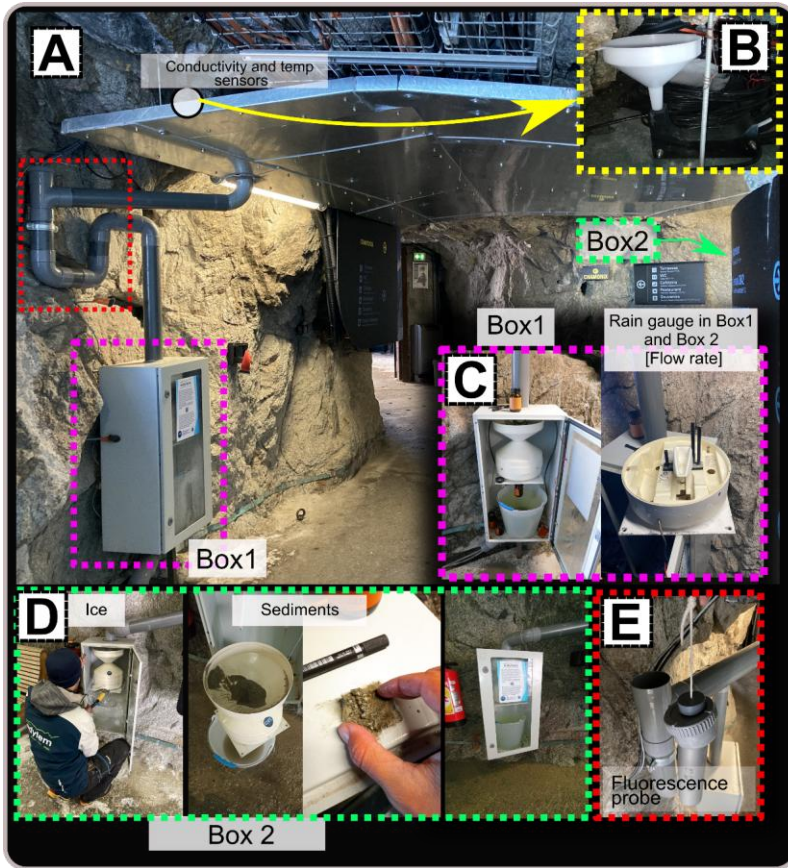
1.8.3.3. Water flows and temperature monitoring in the tunnel

We installed a real-time monitoring system in May 2022 in the west tunnel of the Central Pillar, to characterize the water flowing from fractures that cross the tunnel walls. We took advantage of an existing water diversion ceiling set up by the operating company (Figure 4), made of a convex metallic plate that collects water drips and flows, and diverts them to two pipes, one on each side of the tunnel (east and west) to drain water outside. Preliminary observations revealed that water was mostly dripping from two adjacent fracture systems with a generally subvertical dip (70° - 90°) oriented toward north-west.

The instrumentation included two rain gauges that were installed on each pipe to measure water flow rate (L/h), in protective boxes (Box 1 on the west side and Box 2 on the east side). Water temperature ($^{\circ}$ C) and electrical conductivity (S/cm) were also monitored with sensors placed on the metallic roof, below the identified water drips. The sensors were submerged in a specially designed, 3D printed, siphon-shaped pipe (Figure 4B) to maintain a high water exchange rate and a minimal water level for detection. As a conductivity benchmark, we measured a value of $9.2 \mu\text{S/cm}$ from a melted snow sample collected on the 26 July 2023, which corresponds with known values for snowmelt samples (Brennan et al., 2020; Thompson et al., 2016). In addition, water fluorescence (arbitrary units) was monitored in real-time with a probe inserted in Box 1 to detect the specific emission spectrum of the dye tracer used: Amino-acid-G and sulphorhodamine B in 2022 and Amino-acid-G and Fluorescein in 2023 (see Sect. 3.1 for dye spraying strategy). The fluorescence sensor installed in 2022 (GGUN FL-24) malfunctioned during the 2022 winter and was replaced by a new probe (STREAM model, TRAQUA[®]) on the 31 May 2023. (Brennan et al., 2020; Thompson et al., 2016). In addition, water fluorescence (arbitrary units) was monitored in real-time with a probe inserted in Box 1 to detect the specific emission spectrum of the dye tracer used: AAG and SRB in 2022 and AAG and FLC in 2023 (see Sect. 3.1 for dye spraying strategy). The fluorescence sensor installed in 2022 (GGUN FL-24) malfunctioned during the 2022 winter and was replaced by a new probe (STREAM model, TRAQUA[®]) on the 31 May 2023 and was removed on the 22nd of August several weeks after the last dye signal was detected.

Average values from the installed sensors were recorded every 10 minutes with a PC400 Campbell Scientific data logger. In addition, data from miniature temperature sensors (iButtons, Mouser[®]) that were previously installed were used to monitor the tunnel wall (bedrock) temperature.

The site was visited weekly, excluding a short period from 25 July 2023 to 10 August 2023 because of a storm that prevented access, to retrieve data, take water samples and manual measurements on electrical conductivity, and to clean the rain gauge, since sediments sometimes accumulated (Figure 4).



224

225 Figure 4: Real-time monitoring system in the tunnel. A) The metal roof and Box 1 (pink dashed frame). B) A 3D printed siphon
 226 that was placed directly under the water output from the fracture, equipped with temperature and conductivity sensors (yellow
 227 dashed frame). C) Box 1 interior with rain gauge to monitor flow rate, a sampling bottle, and a bucket. D) Box 2 with sediments
 228 (green dashed frame). E) Fluorescence probe by TRAQUA located in a specially designed siphon for continuous real-time
 229 monitoring of the dye tracers.

230 4.9.3.4. Water sampling in the tunnels and laboratory analysis

231 Water samples were collected weekly from Box 1 during the melting seasons of both 2022 and 2023. Other locations in the
 232 tunnel (labeled Box 2 and TNL) were sampled occasionally six times in 2022 and weekly in 2023. Samples were taken in 125

233 mL brown glass bottles. During the 2023 season, the electrical conductivity of each sample was measured directly after
234 collection. The bottles were stored in a fridge to minimize biological activity and protect them from light.
235 Further high-resolution fluorescence analysis of the water samples was carried out in a laboratory, using a fluorescence
236 spectrophotometer (Varian Cary Eclipse) to validate the real-time fluorimeter data. The samples were exposed to light whose
237 wavelength spectrum matched the excitation spectrum of the dye tracers used in the experiment: (AAG ex:305 nm/em:447
238 nm, SRB ex:555 nm/em:577 nm, FLC ex:490 nm/em:510 nm). The emission vs. excitation wavelength plots were used to find
239 peaks in emission distribution that corresponded to the presence of the dye tracers.
240 In addition to fluorescence analysis, we performed stable isotope analysis on 11 water samples to determine $\delta^{18}\text{O}$ and δD
241 values. Stable isotopes are widely used in hydrological studies to trace the origin and history of water, as their ratios are
242 sensitive to fractionation during phase changes in the hydrological cycle. Such analyses can reveal important information about
243 water sources (e.g. snowmelt vs. rainfall), transport pathways, and storage times. By comparing the measured isotopic
244 signatures to the Global Meteoric Water Line (GMWL), we can assess whether the water follows typical meteoric patterns or
245 has undergone secondary processes such as evaporation, mixing, or prolonged subsurface residence. Deviations from the
246 GMWL can also indicate elevation effects or seasonal variations in precipitation, making isotope data a valuable complement
247 to physical and chemical tracers in characterizing alpine hydrological systems.

248 1.10.3.5. Data analysis

249 We processed and analyzed the continuous time series data by developing codes in Python3 and MATLAB. All time series
250 were filtered for erroneous values and linearly interpolated to evenly spaced time steps for consistency.

251 1.10.1.3.5.1. Recession curves analysis

252 Recession curves have been studied since the late 19th century (Brutsaert and Nieber, 1977; Tallaksen, 1995) and are commonly
253 used in hydrology to interpret the flow behavior and characteristics of aquifers. A key advantage of this approach is that it
254 allows the derivation of empirical, quantitative parameters that reflect the subsurface drainage. Following work by Boussinesq
255 (1877), Maillet (1905) suggested an exponential analytical solution to describe aquifer drainage behavior:

$$256 \quad Q(t) = Q_0 e^{-\alpha t}, \quad (1)$$

257 where Q is flow rate, t is time, Q_0 is peak flow rate, and α is the recession coefficient. ~~To account for flood recession in a~~
258 ~~channelized flow, we opted for the general form suggested by Brutsaert and Nieber (1977)~~ ~~To account for flood recession in a~~
259 ~~channelized flow, we opted for the general form suggested by Brutsaert and Nieber (1977)~~ that is commonly used for river
260 flood recessions (Brutsaert and Nieber, 1977; Krakauer and Temimi, 2011):

$$261 \quad \frac{dQ}{dt} = -\alpha Q^b, \quad (2)$$

262 which can be integrated and solved for $Q(t)$ as:

$$263 \quad Q(t) = (Q_0^{1-b} - a(1-b)t)^{\frac{1}{1-b}}, \quad (3)$$

264

265 where a and b are constant coefficients. Note that the integration of Equation 2 in the case of $b=1$ corresponds to the form of
266 exponential decay as expressed by Equation 1. Scandroglia et al. (2025) recently applied Maillet's law (Equation 1) to analyze
267 flow in fractures within a permafrost-affected rock wall in the Northern Calcareous Alps, at the German-Austrian border. Their
268 study focused on a 55 m-deep tunnel in karst limestones, where flow paths extend at least 55 m and possibly farther due to
269 tortuosity. In contrast, in our study, flow is confined to widely open, sub-vertical granite fractures with path lengths ranging
270 from 12 m (lower terrace) to 20 m (upper terrace). Additionally, while we define a flow event as the period between a well-
271 defined rise and the following recession of the hydrograph, Scandroglia et al. (2025) defined an event as a flow period
272 beginning with a sudden increase in discharge, independent of the starting value, and ending when the flow returns below a
273 set threshold, potentially including several peaks. They applied a single best-fit curve to their entire dataset, which comprised
274 23 such high-flow events over eight years. Their approach is well suited to rain-controlled conditions. In contrast, our field
275 site at 3840 m a.s.l. is dominated by snowmelt and thus strongly influenced by the diurnal solar cycle. We therefore identified
276 93 well-defined single-peak events for recession-curve analysis over two consecutive seasons. To capture temporal variations
277 in flow characteristics rate, we developed an automated algorithm that fits a separate recession curve to each event, enabling
278 to track changes in flow behavior over time (Figure S2, S4). For each event, the algorithm identifies the recession limb as the
279 interval between the last local maximum and the subsequent return to baseflow. It then isolates the concave segment of this
280 limb (curvature > 0), which corresponds to the exponential decay, and fits the appropriate form of Eq. 1 or Eq. 2. To ensure
281 that only well-defined exponential recessions are included, events with regression fits yielding $R^2 < 0.8$ are discarded. This
282 threshold retains 64% of all detected events (93 out of 144) while excluding cases where noisy or multi-peak recession behavior
283 prevents reliable fitting.

284 1.10.2.3.5.2. Moving window cross-correlation

285 ~~A moving window cross-correlation analysis was performed to~~ quantify the ~~correlations and lag-time~~ temporal relationship
286 between ~~pairs of measured time series, including~~ flow rate, AT, and GST. ~~For each lag time, we performed a moving-window~~
287 ~~cross-correlation analysis based on~~ the Pearson correlation coefficient (PCC) ~~was calculated between one series (Pearson,~~
288 ~~1920). For two time series $x(t)$ and a time-shifted version of the other ($+1$: high correlation, 0 : no correlation, -1 : reverse~~
289 ~~correlation). For example, at a lag time of 0 , $y(t)$, the flow and AT were measured at the same time; at a lag time of $+6$ h, the~~
290 ~~flow series was correlated with the AT series shifted forward by 6 h. PCC value (r) at lag τ was defined as:~~

291

$$292 \quad r(\tau) = \text{corr}(x(t), y(t + \tau)) \quad (4)$$

293 ~~where positive lag values ($\tau > 0$) indicate that variations in x follow those in y after a delay τ . Lag times were evaluated in the~~
294 ~~range of -12 to +12 h in steps with a step of 1 h, consistent with the expected diurnal forcing of temperature and flow. The use~~
295 ~~of cross-correlation analysis to assess time-lagged relationships in hydrological time series is well established (e.g., Delbart et~~
296 ~~al., 2014).~~

297 ~~The~~This analysis was ~~performed in a moving window of applied within successive 24-hour windows starting from~~
298 ~~00:00, without overlapping, which corresponds~~corresponding to the ~~observed dominant~~ daily cycles ~~observed in both flow rate~~
299 ~~hydrograph, and GST and AT. Window size is an important parameter: shorter windows highlight transient events but may be~~
300 ~~sensitive to noise, whereas longer windows yield more stable estimates at the cost of smoothing short-term variability. In this~~
301 ~~study, a temperature. A 24-hour window length of 24 hours was selected~~has been chosen as a compromise between ~~detail and~~
302 ~~stability~~diurnal variability resolution and statistical robustness of the correlation estimates.

303 Prior to analysis, all ~~the~~ time series (time step = 10 minutes) were filtered ~~with~~using a one-hour moving average to reduce
304 high-frequency ~~noise. Only~~instrumental noise. This smoothing window is substantially shorter than the dominant diurnal signal
305 ~~and does not affect the identification of lag times at hourly to multi-hour scales, but improves the stability of the correlation~~
306 ~~estimates.~~

307 ~~To ensure that meaningful diurnal responses were analyzed, only~~ days with a maximum flow rate ~~above~~exceeding 6 L h^{-1} were
308 ~~included, ensuring. This threshold excludes low-flow days dominated by noise or weak signals and focuses the analysis on~~
309 ~~periods with well-defined hydrographs with clear diurnal signals.~~

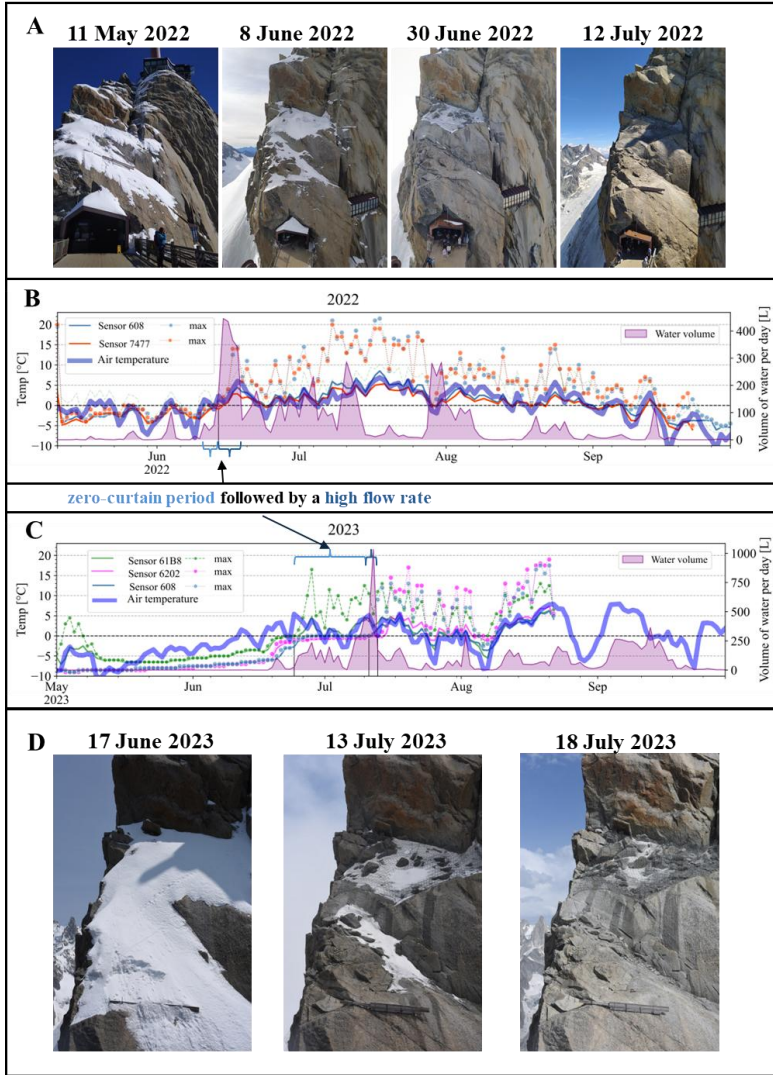
310 The analysis was conducted over the entire flow season (mid-May to August ~~in 2022, and~~ June to September ~~in 2023~~).

311 4. Results

312 4.1.1. Water flow rate

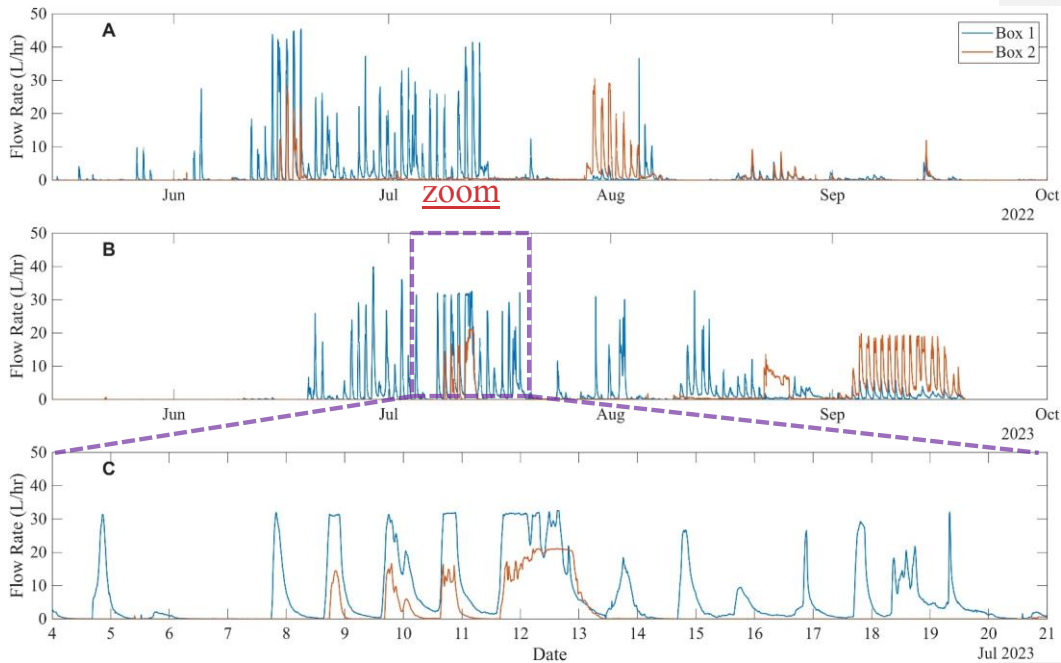
313 Water flow is highly seasonal. In both years, water mostly flowed between May and October, with periods of sporadic and
314 continuous flow that can last several weeks. The occurrence of water flows correlates with the occurrence of positive AT
315 (Figure 5).

316 In 2022, sustained periods of water flow were mainly observed from late May to mid-September, and in 2023, from mid-June
317 to late September. The timing and magnitude of the flow differed between Box 1 and Box 2 (Figure 6). In both years, water
318 flow in Box 1 began several weeks earlier than in Box 2. In general, the amount of water in Box 2 increased throughout the
319 summer season.



322 Figure 5: A) Photos showing the evolution of the snow cover on the NE face during the snow melt season in 2022. B) and C) AT, GST
 323 measured on the NE face, above the tunnel entrance, directly above the monitoring system, and flow rate measured at the output
 324 from rock fractures in the tunnel wall (Box 1+Box 2) in 2022 and 2023, respectively. Solid lines represent the daily average. Note the
 325 zero-curtain period, which marks the melting of the snowpack and the exposure of the rock surface to atmospheric heating. D)
 326 Photos showing the evolution of the snow cover on the NE face during the snow melt season in 2023.

327



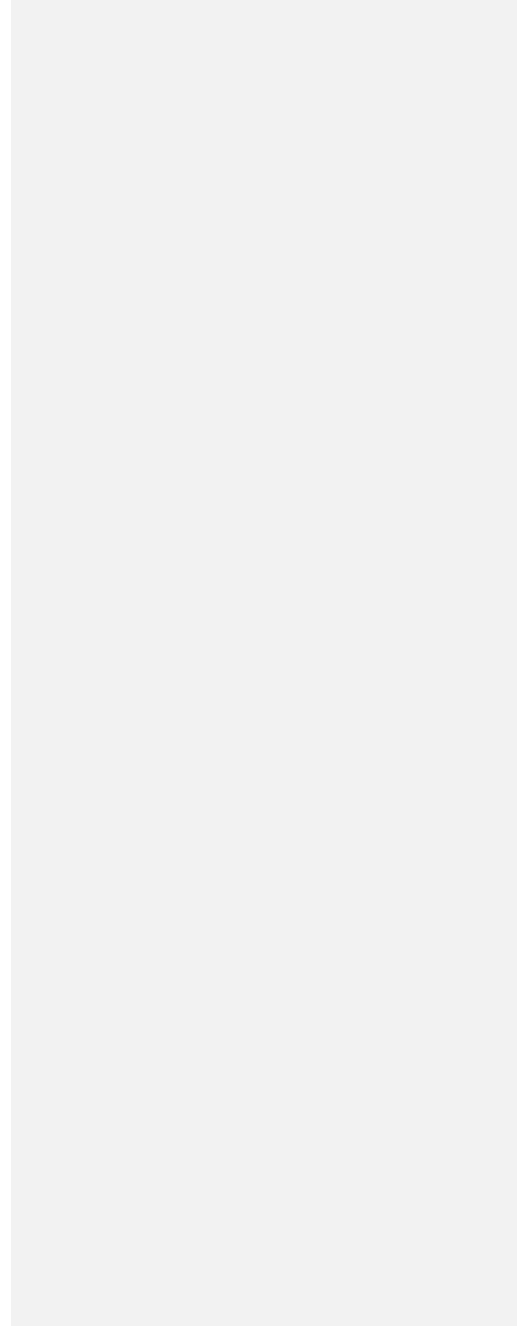
328

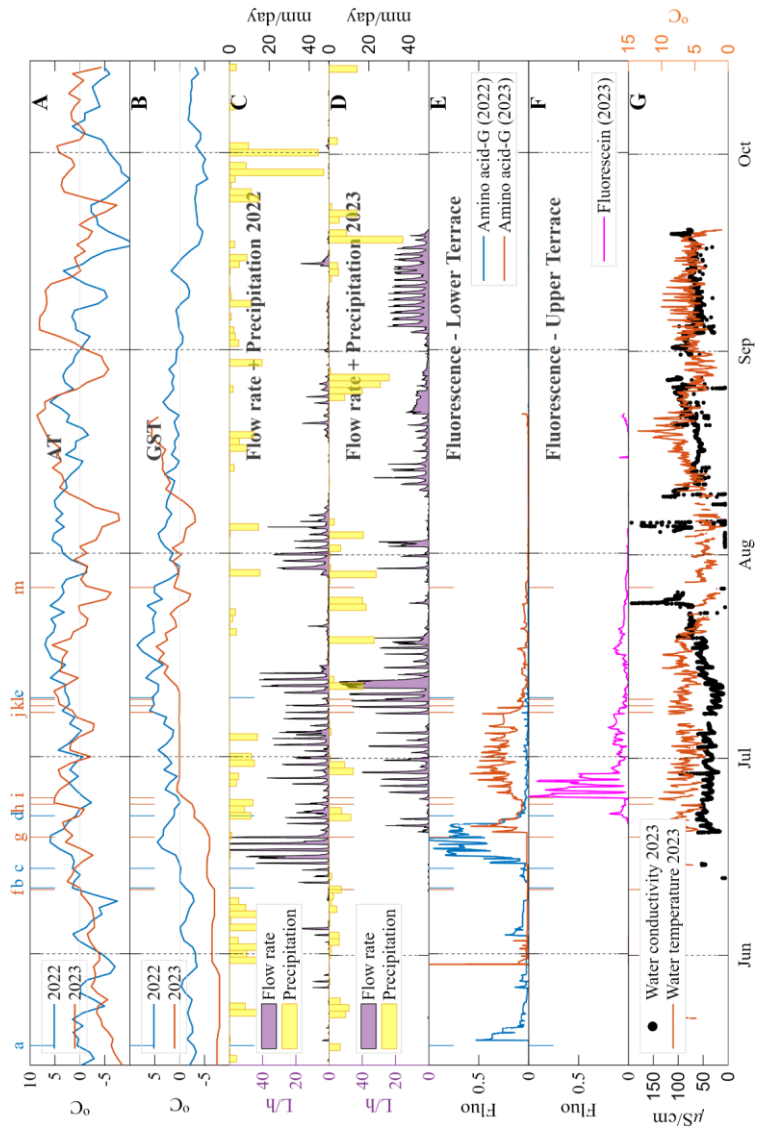
329 Figure 6: A) and B) Time series of flow rate in Box 1 (blue) and Box 2 (orange) during the 2022 and 2023 melt seasons, respectively.
 330 C) Zoom window on the 4-21 July 2023 period.

331 In 2022, the total volume of water flowing through the monitoring system (Boxes 1 and 2) was 8001 L. About 70% of this
 332 volume (5621 L) was collected in Box 1, while the remaining 30% (2380 L) reached Box 2. 75% of the total volume in Box 1
 333 occurred between 11 June and 14 July (4216 L). Of the total flow volume in Box 2, 74% flowed in two relatively short periods:
 334 14 - 19 June (496 L) and 28 July - 8 August (1257 L).

335 In 2023, the total volume of water flow was 11605 L - 45% more than in 2022. Of this, 61% (7079 L) flowed through Box 1,
 336 and 39% (4526 L) in Box 2. 75% of the total volume in Box 1 occurred between 19 June and 10 August (5309 L). In Box 2,

337 almost the entire volume (95%) flowed in three relatively short periods (3 to 18 days): 8 —13 July (831 L), 22—25 August
338 (611 L) and 1—18 September (2851 L).





341 Figure 7: Annual time series. A) Air temperature (AT) measured by Météo-France in Aiguille du Midi. B) Ground surface
 342 temperatures (GST) measured using [miniature temperature sensors \(iButtons\)](#) at the rock surface on rock slope. C-D) Flow rate
 343 measured in both box 1 + box 2 (purple) and daily precipitation measured in Chamonix meteorological station (Météo-France)
 344 (yellow bars). E) Normalized fluorescence signal of amino acid-G dye tracer (2022 and 2023). F) Normalized fluorescence signal of
 345 ~~Sulphorhodamins~~[Sulphorodamine](#)-B (inserted in 2022) and Fluorescein (inserted in 2023) dye tracers. The
 346 ~~Sulphorhodamins~~[Sulphorodamine](#)-B dye was never detected. G) Water conductivity and temperature at the outlet of water from
 347 the fracture in the tunnel. Measurements in time steps without water flow were omitted from the plot. Labeled annotation at the top
 348 of panel A mark the following main events in 2022 (blue): a) first flow event in box 1, b) AT surpasses 0° C, c) GST surpasses 0° C
 349 + beginning of daily oscillations + first flow in box 2, d) amino acid G signal diminishes, e) last amino acid G signal, and 2023
 350 (orange): f) AT surpasses 0° C, g) first water flow event in box 1, h) beginning of daily oscillations, i) beginning of zero curtain, j)
 351 first flow in box 2, k) amino acid G signal diminishes, l) end of zero curtain, m) last amino acid G signal.

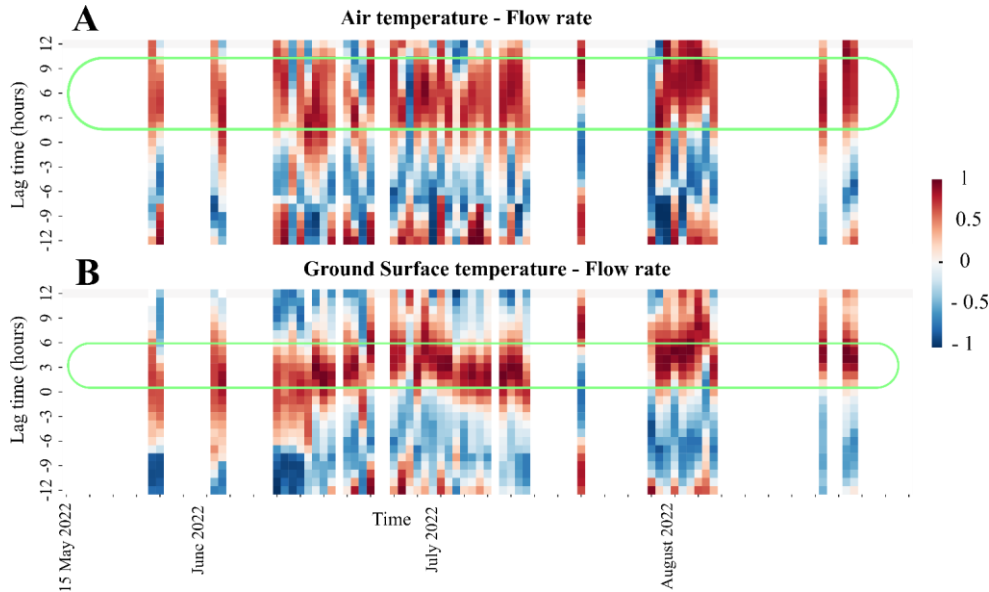
352 The observed flow rate presents daily cycles (Figure 6) with peak flow rates, reaching an order of 10¹ L/h, generally occurring
 353 between 17:00 to 20:00 (Table 2, Figure S1), and minimum flow rates two orders of magnitude lower (order of 10⁻¹ L/h) during
 354 the morning time.

	Average time of signal peak	
	2022	2023
<i>Air temperature (AT)</i>	12:00-15:00	11:00-15:00
<i>Ground surface temperature (GST)</i>	15:30-18:00	15:30-17:00
<i>Flow rate</i>	18:00-19:50	16:20-20:30

355 **Table 22:** Time of day of the daily peak in flow rate, AT, and GST. The listed time ranges represent the 25–75% quantile of daily
 356 peak timing.

357 Results of a moving window cross-correlation show that daily flow rate oscillations are correlated with AT with a lag time of
 358 3-9 hours, and with GST with a lag time of 0-6 hours. This lag time was found to be steady in both years of the experiment
 359 (Table 2, Figure 8).

360



361

362 **Figure 8: Results of moving-window cross-correlation analysis between the water flow rate and the (A) air temperature and (B) the**
 363 **ground surface temperature, during 2022 season. The horizontal axis represents the time (one strip per day), and the vertical axis**
 364 **represents the lag time, in hours. The color bar represents the value of the Pearson correlation coefficient (PCC) (1: high correlation,**
 365 **0: no correlation, -1: reverse correlation). The green frame marks the range of lag times that show high PCC. Results of the cross-**
 366 **correlation analysis of 2023 season show similar results and can be found in the supplementary materials, in figure S3.**

367 In 2022, the first flow in Box 1 was recorded on 15 May (1.1 L/h) and gradually increased, reaching continuous daily flows
 368 with peak values larger than 40 L/h from 11 June -to 14 July, after which flows were linked to rainfall. Box 2 showed its first
 369 significant flow (>10 L/h) on 15 June, with continuous daily oscillations lagging about 5 days behind Box 1. Maximum flow
 370 rates were 45 L/h in Box 1 and 30 L/h in Box 2, with a combined peak of 67 L/h on 16 June.

371 In 2023, Box 1 exhibited continuous daily oscillations from 19 June, peaking at 40 L/h on 28 June, interrupted by short cold
 372 spells, and resuming under positive AT and precipitation events (Figure 6). Box 2 began daily flows between 8–13 July (up to
 373 20 L/h) with a prolonged steady flow (5–12 L/h) from 22–25 August despite minimal precipitation. Maximum individual flows
 374 were 39.83 L/h in Box 1 and 21.20 L/h in Box 2, with combined peak flow of 54 L/h on 12 July. Daily maximum volumes
 375 reached 446 L in 2022 and 1033 L in 2023 (Figure 6).

376

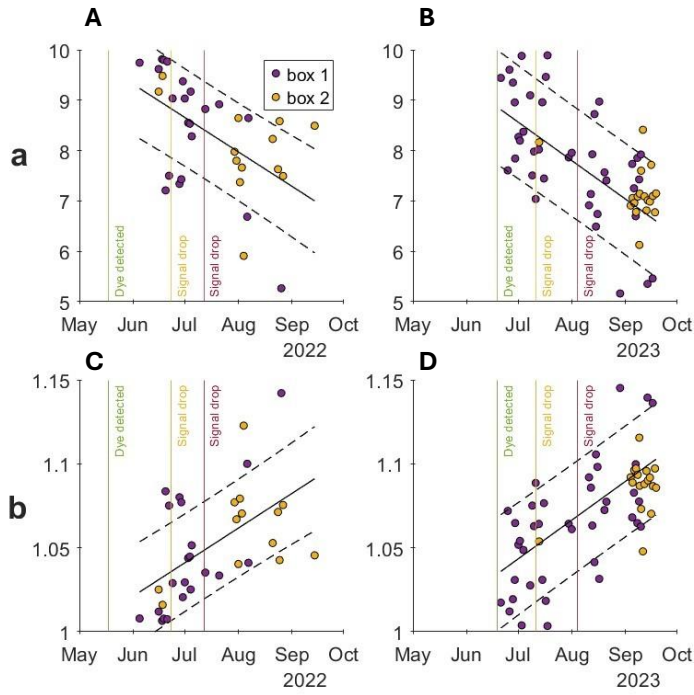
	Peak flow rate (L/h)		Daily max volume (L)
	Box 1	Box 2	
2022	45.4	30.5	446
2023	39.8	21.2	1033

Table 33: Flow rates peaks

The exponential recession curves (Eq.1) fit well with the observed daily events, with an average R^2 value of 0.93. Curves with R^2 values below 0.8 were omitted from the analysis, resulting in 93 events (Figure 9). The 'a' coefficient shows a clear decreasing trend in time from values of 7-10 to 5-8.5 in both 2022 and 2023 seasons (Figure 9), while the 'b' coefficient increases from values of $b \approx 1$ at the beginning of the melting season to values of $b \approx 1.15$ at the end of the season (Equations 2 and 3).

Formatted Table

383



384

385 Figure 9: A-B) values of the 'a' coefficient of the recession curves of flow events in 2022 and 2023 in box 1 (purple circles) and box
386 2 (yellow circles). C-D) values of the 'b' coefficient of the recession curves of flow events in 2022 and 2023 in box 1 (purple circles)
387 and box 2 (yellow circles). Values obtained from curves with R^2 values below 0.8 were omitted from the analysis. The black line is the
388 linear regression of all the points (box 1 + box 2) with \pm standard error (dashed black lines). The vertical lines indicate the timing of
389 the detection of the fluorescent dye in the water that exits the fractures (green), the rapid drop of the signal intensity (orange), and
390 the disappearance of the signal (red).

391

392 4.12.4.2. Snowpack evolution and water flow characteristics

393 Snowpack evolution is assessed through GST measurements at the snow-rock interface and using time-lapse pictures in 2023.

394 Dampened daily oscillations in GST indicate the presence of a snowpack with a significantinsulating significant insulating

395 effect. The melting period is generally visible as a zero-curtain period (*i.e.*, persisting 0 °C conditions at the rock-snow
396 interface) (Hanson and Hoelzle, 2004) that lasts from several days to several weeks.
397 Figure 5 displays the measured GST data at the rock-snow interface [Figure 5](#). In 2022, the dampened daily oscillations are
398 revealed by the similar values of mean and maximum GST, and the zero-curtain period is nearly nonexistent. This could be
399 related to the early heat wave in 2022 that accelerated snow melting. Nonetheless, the first water flow events in May and early
400 June 2022 occurred when GST rose close to 0 °C, demonstrating a link with snow melting. The first significant water flow
401 event in 2022, which is also the greatest one with values reaching over 400 L/day, coincides with the transition to positive
402 GST around mid-June. Summer precipitation episodes are suggested when water flow events follow periods with limited water
403 flow and positive GST and AT, such as in late July 2022. In 2023, the effect of snow cover on GST patterns is more evident,
404 with an initial period of non-existent daily oscillations followed by a zero-curtain period until mid-July. The first flow events
405 occurred during the onset of the snow melting period, with the highest peak of water flow reaching > 1000 L/day at the end of
406 the zero-curtain period.

407 [1.13.4.3.](#) Fluorescence

408 [1.13.4.3.1.](#) Real-time fluorescence monitoring

409 In 2022, the real-time fluorescence sensor shows a strong signal of [amino-acid-GAAG](#) that followed the very first flow events
410 in mid-May 2022 (Figure 7) and the sporadic flow events that followed it until 11 June 2022. The high [amino-acid-GAAG](#)
411 signal continued with the onset of continuous water flows around mid-June 2022, until the rapid decrease at the end of June.
412 The disappearance of the fluorescent signal, despite the sustained water flow likely corresponds to the complete melting of the
413 lower terrace snowpack that contained the [amino-acid-GAAG](#) tracer, as seen in the photos from the time lapse camera (Figure
414 5). A weak signal of [amino-acid-GAAG](#) was detected until mid-July 2022 when both the fluorescence and flow rates
415 diminished. This period of weak [amino-acid-GAAG](#) signal in the water could indicate dilution with water from precipitation
416 that occurred after the dye was inserted or another not-dyed source (either late snow or rain). No signal of the [sulphorhodamine-](#)
417 [BSRB](#) tracer inserted in the upper ledge was found. This could be due to excess dilution of the tracer solution with the snowmelt
418 water to concentrations that were below the sensor sensitivity. A second hypothesis is that snowmelt from the upper terrace
419 did not reach the fracture. In 2023, the [amino-acid-GAAG](#) signal was also detected in the first water flows on 19 June. From
420 the 24 June 2023 onwards, the signal of the [fluorescein-FLC](#) dye was detected alongside [amino-acid-GAAG](#), which likely
421 confirms that the concentration in [sulphorhodamine-BSRB](#) was probably too low in 2022. The [fluorescein-FLC](#) signal is shorter
422 than the [amino-acid-GAAG](#) signal, with a single high peak in the last week of June followed by a rapid decrease to low values.
423 This could be explained by the different pathways from the upper terrace snowpack through the fracture network, together
424 with the effect of low dispersivity of [fluorescein-FLC](#). The high peaks of [amino-acid-GAAG](#) persisted continuously until 8
425 July. Afterward, both tracers remained in low concentrations until the end of July, suggesting that much of the winter and

426 spring snow had melted by 27 July. That could mean that the time needed for the entire winter snowpack to infiltrate is slightly
427 more than a month. After that, the water flowing from mid- to late July was either direct precipitation (rain and snow) or
428 possibly meltwater from ice that predated the tracer insertion.

429 1.13.2.4.3.2. Fluorescence laboratory results

430 Additional analyses of water samples collected between May and mid-July 2023 from Boxes 1 and 2 and various fractures
431 dripping into the tunnels of AdM were carried out using a high sensitivity spectrophotometer in the EDYTEM laboratory. The
432 results are similar and confirm those found using the TRAQUA real-time sensor in Box 1. The signals for ~~Fluorescein~~FLC
433 and ~~amino-GAAG~~ show peaks at the same periods, i.e. at the end of the month of June and the beginning of July. The
434 ~~fluorescein~~FLC signal is very short-lived, unlike ~~amino-GAAG~~, which continues to appear for a longer period. Samples from
435 other locations in the tunnel show no signal of any of the fluorescent dyes.

436 1.14.4.4. Stable isotopes

437 Analysis of oxygen and hydrogen isotopes in the water samples shows that $\delta^{18}\text{O}$ and δD values range between -3.2‰ to -10‰
438 and -15‰ to -73‰ respectively (Figure 10). Excluding two samples, the $\delta^{18}\text{O}/\delta\text{D}$ ratio in all the water samples fall close to
439 the global meteoric water line (GMWL) or align on a straight line parallel to the GMWL, likely because of a seasonal evolution
440 of the local meteoric line from the GMWL (i.e. three samples taken on 22 September -labeled _22SEP). Two samples taken
441 on 28 July 2022 from Box 2 deviate significantly below the GMWL (BOX2_28JUL – directly from the fracture,
442 BCKT2_28JUL – from a 5L bucket that collected the water from the fracture) (Figure 10). This suggests that the water
443 emerging from the fracture above Box 2 on that day was not of recent meteoric origin.

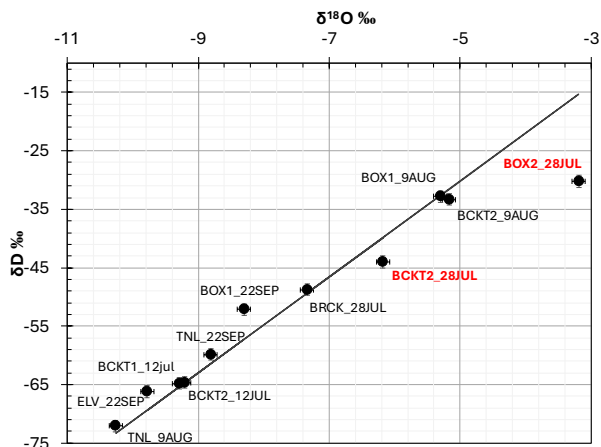


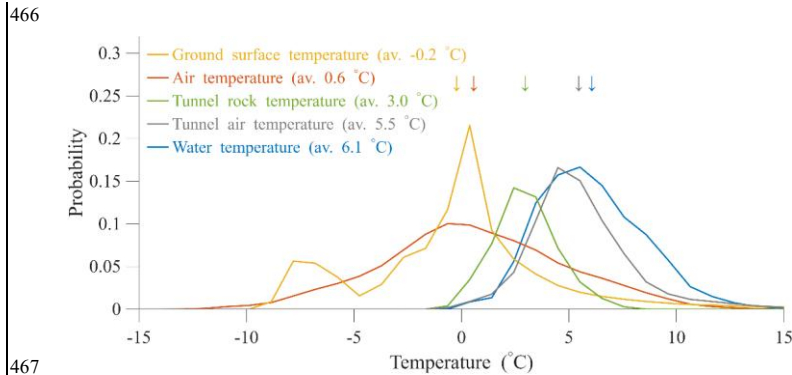
Figure 10: Stable isotopes $\delta^{18}\text{O}$ and δD in water samples. Note the two outliers (labeled in red) from the global meteoric water line (GMWL, black line) in samples taken from Box 2 on 28 July 2022.

1.15.4.5. Water electrical conductivity

Electrical conductivity values are provided as maximum values per day of flow, after correction to a standard temperature of 25°C. The electrical conductivity measurements from the 2022 season were unreliable due to the erroneous installation of the sensor. Therefore, only the 2023 results are presented and analyzed (Figure 7). Overall, the conductivity values were far above the benchmark value measured in melted snow samples (9.2 $\mu\text{S}/\text{cm}$). On the continuous measurement (real-time monitoring system), the electrical conductivity of the water flowing into Box 1 remained relatively constant from mid-June to mid-July, with daily oscillations between 10-55 $\mu\text{S}/\text{cm}$ and a general decreasing trend. The daily oscillations correlate with flow rate in a reverse relation – when flow rate is high the conductivity decreases (Figure 7). These values of conductivity correspond to the period of continuous cyclic flow rate in Box 1 that ended with the complete thaw of the winter snowpack. Interestingly, significantly higher conductivity values were measured at other locations in the tunnels. Conductivity measurements with values of 485 $\mu\text{S}/\text{cm}$ were taken in a tunnel wall under the west face of the central peak, from mid-July onwards, and 430 $\mu\text{S}/\text{cm}$ (measured in 2022) at another location in a tunnel under the north-east face of the central peak, near the exit of the cable car going to Pointe Helbronner (Italy).

460 **1-16.4.6. Water temperature**

461 During flow events, the water temperature measured in two locations at outputs from the fractures ~~ranges~~ ranged between 0 °C
462 and 13 °C with an average of 6.1 °C (Figure 11). Measurements taken during periods without flow or subzero temperatures
463 were removed from the analysis. Average GST and AT during the thawing season (15 May to 15 September) are close to 0 °C.
464 Values measured at the rock surface in the tunnel walls, near the fractures, during flow events show an intermediate mean
465 value of 3.0 °C.



468 **Figure 11: Probability distribution of temperatures monitored during flow events (blue), atmospheric ATs (orange), ground surface**
469 **temperatures (yellow), tunnel wall (green), and tunnel air. All distributions show data from the thawing season in 2022 and 2023 (15**
470 **May – 15 September). Note that the water temperature distribution (blue) shows only data when water flow was detected in the**
471 **monitoring system, while the other temperature distributions represent the entire data within the thawing season. The arrows show**
472 **the location of the mean values on the horizontal axis.**

473 **5. Discussion**

474 **1-17.5.1. Water flows and weather conditions**

475 Our results show rare evidence of highly effective surface-subsurface connectivity in steep permafrost-affected slopes, and
476 strong weather signals in both seasonal and diurnal scales. There is a clear link between the timing of AT and GST becoming
477 positive in the early summer months and the onset of water flow. The first flow events in the season, which appeared in early
478 May (2022) and June (2023), display a clear signal of the dye tracer and are directly linked to snow melting occurring under
479 positive AT in the relatively shaded north-exposed rock face.

480 In both years, the onset of water flow in the fractures occurred when the daytime AT reached values above 0 °C. This change
481 in temperature to positive values directly induced the melting of the snow that was deposited during winter, and its infiltration
482 into the fractures. The melting of the snowpack is demonstrated by the simultaneous detection of the fluorescent dye tracers

483 injected into the snowpack and the zero-curtain effect observed in the GST (Figure 5, Figure 7). The melting accelerated when
484 the rock surface was exposed to heat flux from the atmosphere and GST turned positive. From this point onwards, water flow
485 behavior became more uniform, with regular daily oscillations, and reached the highest flow rates. Subsequently, after the
486 exposure of the rock surface, some of the water in the fracture was directly from precipitation, which likely melted rapidly on
487 the rock surface as the temperature increased, often above 0 °C. Each year, water flow in the fractures ceased when the
488 temperature became negative again in autumn, with icicles appearing in the fractures.

489 Based on the 2-year monitoring, we conclude that water flow processes in high mountain rock faces are therefore seasonal,
490 directly linked to the change in air and surface temperatures to above 0 °C during the summer period and below 0 °C during
491 fall. The continuous detection of the dye, together with an analysis of time-lapse photos of the rock face and the shift of GST
492 to positive values, show that snowmelt is the main source of water in the fractures during the early and main stages of flow,
493 and contributes most of the water. This is consistent with similar observations reported by Scandroglio et al. (2025)(2025).

494 GST and AT also control flow rate oscillations on a daily time scale and are cross-correlated with a lag time of 3-9 and 0-6
495 hours, respectively (Table 2, Figure 8, Figure S3). These lag times provide an estimation of the time taken for water to travel
496 through the fracture system, and allow a rough approximation of flow velocity on the order of ~10 m/hr.

497 The observed acceleration in flow rate coincides with the heating of the rock surface to above 0 °C and points to a top-down
498 thawing of the active layer (i.e. the near-surface layer that freezes and thaws through summer).

499 Nevertheless, the time lag between surface signal and water flow as well as the thawing of the active layer must be cautiously
500 considered as it is possibly influenced by the open-system of the tunnel causing an open flow path and a thermal shortcut
501 allowing for bottom-up heat transfer. In addition, the touristic infrastructure and human presence can contribute to internal
502 heat sources, including heating systems, the elevator motor, and body heat from visitors (Figure 11).

503 **1.17.1.5.1.1. Heat waves effect**

504 The contrast in summer conditions between 2022 and 2023 further illustrates the strong influence of weather conditions on the
505 timing and characteristics of the water flow period (Sect. 2.2)2.2). This is well demonstrated by the effect of the early heat
506 wave in spring 2022 that resulted in an early onset of water flows and the late heat wave in autumn 2023 that extended the
507 water flow period much later in the season. The 2023 season was significantly wetter in terms of precipitation, and
508 subsequently, more water flowed in the monitored fractures. However, comparing the monthly distribution of flow during the
509 thawing season reveals that it was greatly influenced by the heat waves. Between May to mid-July, flow volume in 2022 was
510 much higher than in the same period in 2023, as a result of the early and rapid thawing. Only in late August, did the total
511 volume of water flow surpass that of 2022. This raises an interesting point for future research on the influence of early vs. late
512 water infiltration in permafrost rocks and the impact on hillslope processes. Assuming that water that infiltrates later in the
513 season is warmer than the rock mass, and the infiltration paths contain less ice, it can potentially accelerate permafrost
514 degradation and thickening of the active layer.

515 Compared to the less extreme spring temperatures in 2023, the rapid thaw in 2022 is evident in the GST data and in the absence
516 of a zero-curtain period, which is clearly observed in 2023 (Figure 5, Figure 7). We suggest that during the early heatwave in
517 2022, there was less snow, the thawing was very rapid, and the latent heat was absorbed rapidly. This can be seen in Figure 5,
518 which shows less snow cover in mid-June 2022 in comparison with mid-June 2023, and a large volume of water immediately
519 after GST turns positive.

520 4.18.5.2. Water flow path conditions

521 Our results also indicate that an effective pathway exists within the fracture network through which the water released by
522 snowpack melt can infiltrate at the end of spring. The early detection of fluorescent dye in the first flow events suggests a
523 relatively rapid transfer from the surface to the fractures. Furthermore, when flow ceases at the end of autumn and icicles form
524 at the fracture outlet, the observed flow appears to be unsaturated. In such cases, the unsaturated flow is likely routed through
525 preferential pathways within the fracture system, which in turn suggests that at least part of the network remains open and able
526 to convey meltwater during the following spring. However, we cannot overrule the possibility that the man-made space of the
527 tunnel contributed to the unsaturated conditions. In natural conditions, if undrained conditions occur, water could accumulate
528 in the fractures, refreeze inside them, and seal them off. Artificial prevention of ice accumulation can inhibit fracture
529 development through ice segregation and the related cryostatic pressure (Draebing et al., 2014; Draebing and Krautblatter,
530 2019; Hales and Roering, 2007; Hallet et al., 1991; Matsuoka and Murton, 2008; Matsuoka and Sakai, 1999)(Draebing et al.,
531 2014; Draebing and Krautblatter, 2019; Hales and Roering, 2007; Hallet et al., 1991; Matsuoka and Murton, 2008; Matsuoka
532 and Sakai, 1999). Completing these water flow observations with crack-meters to measure fracture rheology would provide
533 an interesting perspective to clarify the role of the tunnel. However, this would require ~~to identify~~identifying the fractures that
534 are directly connected to the tunnel.

535 Interestingly, our monitoring system shows different but consistent timing of water flows in Boxes 1 and 2, despite them being
536 located only a few meters apart (Figure 6). One reason for the delayed flow in Box 2 could be linked to the location of the
537 draining area closer to the colder north face, while the draining area of Box 1 is closer to the west face, which receives more
538 solar radiation. Another explanation could be suggested based on the observed accumulation of sediments in Box 2, which
539 was not observed in Box 1. The origin of the sand-size sediments observed in Box 2 is very likely from the erosion of the
540 granite rock. This suggests that the fracture system drained to Box 2 is filled with sediments that reduce the hydraulic
541 conductivity. However, once flow begins in Box 2, it responds directly to precipitation and positive AT and reaches high flow
542 rates, similar to those measured in Box 1 (e.g. in September 2023, Figure 6, Figure 7). This supports the first hypothesis of
543 different exposures to solar radiation. The effect of the sediments filling on the hydraulic conductivity is thus reduced in late
544 summer, perhaps due to the thawing of ice-filled pores within the sediments filling. Alternatively, the sand and ice in the sub-
545 vertical fractures might act as a partial plug that accumulates water above the infill. When the hydraulic head is high and the

546 ice filling is thawing, the plug can break, allowing the sand to be transported, and causing a change in the flow regime (as it
547 was observed in Box 2).

548 Based on the delayed onset of flow into Box 2 and the different flow behavior when compared with Box 1, we suggest that the
549 two boxes collect two different flow pathways which have some common parts. As Box 1 and Box 2 are located approximately
550 3 m apart, we suggest that the fracture network is complex under the north face. Some parts of the network contain sand-size
551 sediments, which probably explain the late and lower flow of Box 2. Other parts of the network lack sand filling and have a
552 different hydraulic behavior. The effect of the sediment infill on fracture hydrology should be investigated further.

553 4.19.5.3. Deciphering possible water sources

554 According to the fluorescence data and the water flow timing, much of the collected water originates directly from recent
555 snowmelt. This is also supported by the stable isotopes analysis of water samples from Box 1 (Figure 10) which display values
556 that are consistent with those reported in high-elevation mountain regions, such as the Alps (Lauber and Goldscheider, 2014),
557 the Pyrenees (Herms et al., 2019), and Northern China mountains (Sun et al., 2016). It is also very likely that rain in late
558 summer infiltrated the rock fractures and contributed to the flow. However, some data also hints at other possible sources of
559 water. First, even the lowest values of electric conductivity of the water are far above the expected snow melt conductivity and
560 they steadily rise with decreasing flow rate. The surprisingly high electric conductivity found in some samples collected from
561 fractures ($>400 \mu\text{S}/\text{cm}$) can point to long residence times in the rock. Considering the results from the fluorescent dyes and
562 the hydrological behavior, the flow path is very short (in both distance and time), thus ruling out a long exchange time between
563 the surface water and the rock. It is possible that recent meteoric water was mixed with older water that was trapped as ice in
564 the permafrost-affected rocks. This is also supported by the observed change in the shape of the recession curves over time
565 (Figure 9). The recession curves at the beginning of the melting season (May-June) show values of $b \approx 1$ and fit well with the
566 exponential form that is expressed in Equation 1. The early-season recession curves are also characterized by high values of
567 'a'. Over time, the value of 'b' increases linearly to a form better described by Equation 3, while the value of the 'a' coefficient
568 decreases. This change in recession form (Figure S4), from aquifer-type (Equation 1) to channel-type (Equation 3) can be
569 explained by the thawing of ice in wide sub-vertical fractures that are likely to react more individually (rather than as a network)
570 and enable rapid flow in the fractured granite. The decrease of 'a' is non-trivial since one could expect that the drainage would
571 be more efficient and with shorter recession time (i.e. higher 'a' values) as the thawing of ice in the rock fractures progresses.
572 We thus suggest that the observed decrease in 'a' is due to a gradual change in the water source. As less water drains from the
573 surface (after the complete thawing of the winter snow) and more water drains from the subsurface ice trapped in the fractures,
574 the hydraulic gradient is reduced, and the duration of the recession is extended. Another evidence of a possible fossilized
575 source can be seen in samples collected from Box 2 on 28 July (BOX2_28JUL, BCKT2_28JUL) which show an isotopic signal
576 that is distant from the meteoric water line (Figure 10). One possible explanation is an extended residence time within the
577 fracture system, allowing for interactions with the surrounding rock. Water samples collected during the peak of summer, on

578 July 28 (BOX2_28JUL, BCKT2_28JUL) and August 9 (BOX1_9AUG, BCKT2_9AUG), from both collection systems (Box
579 1 and Box 2) exhibit relatively enriched $\delta^{18}\text{O}$ and δD values compared to those taken in early summer and fall. This enrichment
580 may indicate the partial melting of seasonal snow. In contrast, two other samples from different locations within the AdM
581 tunnels (TNL_9AUG and BRCK_28JUL), collected on the same dates, do not show this enrichment. The observed $\delta^{18}\text{O}$ and
582 δD enrichment during summer is consistent with findings from the Alps (Lauber and Goldscheider, 2014; Novel, 1995).

583 From a permafrost perspective, the thawing of large volumes of fossilized water in permafrost-affected rock could be related
584 to a thickening of the active layer and degradation of high mountain permafrost - a regional phenomenon seen in recent decades
585 in boreholes in the Alps and other mountain ranges (Magnin et al., 2024; Noetzli et al., 2024), but never observed directly in
586 water samples from fractures.

587 The absence of a signal from [sulphorhodamine-BSRB](#) tracer in the water from the upper ledge could be due to excess dilution
588 of the tracer solution with the snowmelt water, resulting in concentrations below the sensor sensitivity. In 2023, a different
589 dye was used ([fluoresceinFLC](#)), with a significantly higher concentration (see Sect. 3.1), and was clearly detected, confirming
590 that the absence of a [sulphorhodamine-BSRB](#) signal in 2022 was due to dilution.

591 [1.20.5.4.](#) **Implications for alpine geomorphology, hydrogeology, and permafrost**

592 The quantity, timing, and characteristics of water that infiltrates in the fractured, permafrost-affected rocks are important
593 factors in many geomorphological, hydrological, and geomechanical processes. However, our understanding of the parameters
594 controlling these factors is limited, as is the ability to measure them. For example, the timing and quantity of water availability
595 from snowmelt are often estimated indirectly using numerical models of energy and water mass balance ([Ben-Asher et al.,
596 2023; Lehning et al., 1999; Leinauer et al., 2021](#))([Ben-Asher et al., 2023; Lehning et al., 1999; Leinauer et al., 2021](#)) and
597 snowpack physics (Lehning et al., 1999; Vionnet et al., 2012). However, the outputs of such models depend strongly on the
598 meteorological forcing used to drive them, and on hydrogeological parameters that are usually poorly constrained. The results
599 of this study provide direct observations that can help to reduce these uncertainties and improve our understanding of water
600 availability for infiltration and its environmental controls.

601 The new information that we provide regarding water flow in permafrost rock fractures can also be used to improve coupled
602 heat and water flow models, as it provides the parameters needed to calculate heat advection from the surface (flow rate and
603 water temperature). The average water temperature measured during flow events is 6.1 °C (Figure 11). ([Magnin and Josnin,
604 2021](#))

605 Several recent studies suggest that water-related processes are driving rockwall instability in mountain permafrost ([Cathala et
606 al., 2024; Gruber et al., 2004; Krautblatter et al., 2012; Magnin and Josnin, 2021](#))([Cathala et al., 2024; Gruber et al., 2004;
607 Krautblatter et al., 2012; Magnin and Josnin, 2021](#)). Analysis of 1152 rockfall events in the Mont Blanc massif between 2015-
608 2021 ([Magnin et al., 2023; Ravanel and Deline, 2013](#))([Magnin et al., 2023; Ravanel and Deline, 2013](#)) shows that 96% of the

609 events occurred between June and September, with the highest numbers in July, before the maximum depth of the seasonal
610 active layer was reached (Magnin et al., 2023), possibly due to enhanced water flows when snow melts in the early summer.

611 The cable car to AdM has been operating since the 1950s. The staff of the company operating ~~company of~~ the site reported
612 that significant water flow from the fractures in the tunnel began in the particularly hot summer of 2015. While the reason for
613 the initiation of the observed seasonal flow remains unclear, it is reasonable to suggest that it is related to the gradual heating
614 of the rock mass in AdM and the development of the active layer that is observed in monitored boreholes in the site (Magnin
615 et al., 2024). This suggests that the environmental conditions in AdM are in a transient state and have reached a threshold that
616 triggers substantial water availability to fractures in the permafrost rocks.

617 4.21.5.5. Outlook and Future Directions

618 Future investigations could build upon this study by conducting more detailed chemical analyses of dissolved elements, which
619 would help constrain water–rock interaction processes and potential solute sources. Characterizing the mineralogy and size
620 distribution of sediments flushed from fractures could provide complementary evidence regarding transport pathways and
621 mechanical erosion. Further stable isotope analyses, combined with absolute dating techniques (e.g., tritium–helium,
622 radiocarbon, or noble gas methods), could enable a clearer distinction to be made between modern meltwater, rainfall, and
623 contributions from older subsurface ice. Together, these approaches would refine our understanding of fracture-scale
624 hydrology in steep permafrost rock walls and how sensitive it is to climate change.

625 6. Conclusions

626 This study presents novel, direct observations of water infiltration in a high mountain permafrost rock wall, providing rare
627 field data on processes that are typically poorly understood and rarely monitored. A two-year monitoring system was installed
628 inside man-made tunnels at the Aiguille du Midi (3842 m a.s.l.) in the Mont Blanc massif to track real-time water flow,
629 temperature, electrical conductivity, and the infiltration of fluorescent tracers injected into the overlying snowpack. These
630 measurements were then combined with GST and meteorological data to investigate the origin, timing, and dynamics of water
631 flow in permafrost-affected fractured rock.

632 Our main findings are:

633 • Water flow in fractures is seasonal and begins when AT exceeded 0 °C. Steady flow with daily oscillations began when
634 GST rose above 0°C, which occurred several weeks (in 2022) or days (in 2023) after the initiation of flow.

635 • ~~This flow contained the dye tracer that had been inserted into the snowpack above the tunnel.~~

636 • Fluorescent tracers were detected in the first water flow ~~in early summer~~ and in the ~~flow that followed~~ subsequent flows
637 until mid-summer. This confirms that the main source of water is snowmelt from the winter snowpack. During late

Formatted: Outline numbered + Level: 1 + Numbering Style:
Bullet + Aligned at: 0 cm + Tab after: 0 cm + Indent at:
0.63 cm

Formatted: Outline numbered + Level: 1 + Numbering Style:
Bullet + Aligned at: 0 cm + Tab after: 0 cm + Indent at:
0.63 cm

638 ~~summer, once the winter snowpack had disappeared, water flow was related to snow or rain events and did not show~~
639 ~~tracers signal.~~

640 ~~• In snow-free conditions, during late summer, rain also contributes to the flow.~~

641 • The daily peak flow rate shows short lag times relative to the peaks of air and ground temperatures (3–9 h and 0–3 h,
642 respectively), indicating rapid, unsaturated infiltration pathways.

643 • Evidence from electrical conductivity measurements, stable water isotopes, and analysis of recession curves suggests that
644 water stored in the rock is contributing to the flow, possibly from the melting of older ice within the fracture system.
645 Further investigation is needed to determine the origin of water with high electrical conductivity and a unique isotopic
646 signature. However, if confirmed, it would provide direct evidence of the melting of fossil ice and permafrost degradation.

647 • Distinct flow regimes of flow collected from two nearby fractures in Boxes 1 and 2 demonstrate a heterogeneous fracture
648 network with varying sediment infill. It reveals the existence of fractures directly linked to the surface on the one hand,
649 and fractures with sand infill and likely ice fill with a longer transfer time on the other hand. Moreover, the hydraulic
650 characteristics of the fractures show unsaturated flow with preferential paths at the end of each warm season before the
651 active layer freezes again.

652 ~~• Water temperatures often exceed 5 °C; together with the intense water flow measured, it strongly suggests that advective~~
653 ~~heat transfer likely contributes to ice melting within the rock mass.~~

654 This work provides direct empirical evidence of how surface water infiltrates permafrost rock walls and interacts with the
655 surface and internal fracture systems. These findings are crucial for the development of coupled hydro-thermal models and
656 understanding how climate warming affects permafrost degradation, water pathways, and slope stability. This approach and
657 its results can help future studies that aim to characterize hydrogeological processes in high-elevation rock fractures, identify
658 early signs of geomorphic instability, and assess the vulnerability of alpine permafrost landscapes in the context of ongoing
659 climate change.

660 **Author contribution**

661 MB, JYJ, FM: Conceptualization, Data curation, Investigation, Formal analysis, Methodology, Writing.

662 AC: Data curation, Investigation, Formal analysis, Methodology, Writing.

663 JB: Investigation, Writing.

664 EM: Investigation, Methodology.

665 AP: Resources.

666 YP: Data curation, Methodology.

Formatted: Outline numbered + Level: 1 + Numbering Style:
Bullet + Aligned at: 0 cm + Tab after: 0 cm + Indent at:
0.63 cm

667 **Competing interests**

668 The authors declare that they have no conflict of interest.

669 **Acknowledgements**

670 We thank the Compagnie du Mont Blanc and the Aiguille du Midi station staff for their support and access to the site. We also
671 thank UMR 1114 EMMAH laboratory (Environnement Méditerranéen et Modélisation des Agro-Hydrosystèmes) for the stable
672 isotope analysis. We are grateful for the assistance of Marine Quiers in planning and applying fluorescence techniques. This
673 research has been supported by the Agence Nationale de la Recherche (WISPER project, no. ANR-19-CE01-0018).

674 **References**

675 Allen, S. K., Gruber, S., and Owens, I. F.: Exploring steep bedrock permafrost and its relationship with recent slope failures
676 in the Southern Alps of New Zealand, *Permafr. Periglac. Process.*, 20, 345–356, <https://doi.org/10.1002/ppp.658>, 2009.

677 Bast, A., Kenner, R., and Phillips, M.: Short-term cooling, drying, and deceleration of an ice-rich rock glacier, *The Cryosphere*,
678 18, 3141–3158, <https://doi.org/10.5194/tc-18-3141-2024>, 2024.

679 Ben-Asher, M., Magnin, F., Westermann, S., Malet, E., Berthet, J., Bock, J., Ravel, L., and Deline, P.: Estimating surface
680 water availability in high mountain rock slopes using a numerical energy balance model, [https://doi.org/10.5194/esurf-11-899-](https://doi.org/10.5194/esurf-11-899-2023)
681 2023, 2023.

682 Boussinesq, J.: *Essai sur la théorie des eaux courantes*, Impr. nationale, 1877.

683 Brennan, K. P., David, R. O., and Borduas-Dedekind, N.: Spatial and temporal variability in the ice-nucleating ability of alpine
684 snowmelt and extension to frozen cloud fraction, *Atmospheric Chem. Phys.*, 20, 163–180, [https://doi.org/10.5194/acp-20-163-](https://doi.org/10.5194/acp-20-163-2020)
685 2020, 2020.

686 Brutsaert, W. and Nieber, J. L.: Regionalized drought flow hydrographs from a mature glaciated plateau, *Water Resour. Res.*,
687 13, 637–643, <https://doi.org/10.1029/WR013i003p00637>, 1977.

688 Cathala, M., Bock, J., Magnin, F., Ravel, L., Ben Asher, M., Astrade, L., Bodin, X., Chambon, G., Deline, P., Faug, T.,
689 Genuite, K., Jaillet, S., Josnin, J.-Y., Revil, A., and Richard, J.: Predisposing, triggering and runout processes at a permafrost-
690 affected rock avalanche site in the French Alps (Étache, June 2020), *Earth Surf. Process. Landf.*, 49, 3221–3247,
691 <https://doi.org/10.1002/esp.5881>, 2024.

692 Copernicus Climate Change Service (C3S): European State of the Climate 2022, Copernicus Climate Change Service (C3S),
693 <https://doi.org/10.24381/GVAF-H066>, 2023.

694 Copernicus Climate Change Service (C3S): European State of the Climate 2023, Copernicus Climate Change Service (C3S),
695 <https://doi.org/10.24381/BS9V-8C66>, 2024.

- 696 [Delbart, C., Valdes, D., Barbecot, F., Tognelli, A., Richon, P., and Couchoux, L.: Temporal variability of karst aquifer response](#)
697 [time established by the sliding-windows cross-correlation method, *J. Hydrol.*, 511, 580–588,](#)
698 <https://doi.org/10.1016/j.jhydrol.2014.02.008>, 2014.
- 699 Deline, P., Gruber, S., Delaloye, R., Fischer, L., Geertsema, M., Giardino, M., Hasler, A., Kirkbride, M., Krautblatter, M.,
700 Magnin, F., McColl, S., Ravel, L., and Schoeneich, P.: Ice Loss and Slope Stability in High-Mountain Regions, in: Snow
701 and Ice-Related Hazards, Risks, and Disasters, Elsevier, 521–561, <https://doi.org/10.1016/B978-0-12-394849-6.00015-9>,
702 2015.
- 703 Draebing, D. and Krautblatter, M.: The Efficacy of Frost Weathering Processes in Alpine Rockwalls, *Geophys. Res. Lett.*, 46,
704 6516–6524, <https://doi.org/10.1029/2019GL081981>, 2019.
- 705 Draebing, D., Krautblatter, M., and Dikau, R.: Interaction of thermal and mechanical processes in steep permafrost rock walls:
706 A conceptual approach, *Geomorphology*, 226, 226–235, <https://doi.org/10.1016/j.geomorph.2014.08.009>, 2014.
- 707 Dwivedi, R. D., Singh, P. K., Singh, T. N., and Singh, D. P.: Compressive strength and tensile strength of rocks at sub-zero
708 temperature, *Indian J. Eng. Mater. Sci.*, 5, 43–48, 1998.
- 709 Eppes, M. C. and Keanini, R.: Mechanical weathering and rock erosion by climate-dependent subcritical cracking, *Rev.*
710 *Geophys.*, 55, 470–508, <https://doi.org/10.1002/2017RG000557>, 2017.
- 711 Erismann, T. H. and Abele, G.: *Dynamics of rockslides and rockfalls*, Springer Science & Business Media, 2001.
- 712 Fey, C., Wichmann, V., and Zangerl, C.: Influence of permafrost degradation and glacier retreat on recent high mountain
713 rockfall distribution in the eastern European Alps, *Earth Surf. Process. Landf.*, 50, e70063, <https://doi.org/10.1002/esp.70063>,
714 2025.
- 715 Fischer, L., Amann, F., Moore, J. R., and Huggel, C.: Assessment of periglacial slope stability for the 1988 Tschierwa rock
716 avalanche (Piz Morteratsch, Switzerland), *Eng. Geol.*, 116, 32–43, <https://doi.org/10.1016/j.enggeo.2010.07.005>, 2010.
- 717 Ford, D. and Williams, P.: *Karst geomorphology and hydrology*, 1st ed., Unwin Hyman, London, 42 pp., 1989.
- 718 Gabrielli, C. P., McDonnell, J. J., and Jarvis, W. T.: The role of bedrock groundwater in rainfall–runoff response at hillslope
719 and catchment scales, *J. Hydrol.*, 450–451, 117–133, <https://doi.org/10.1016/j.jhydrol.2012.05.023>, 2012.
- 720 Gardent, M., Rabatel, A., Dedieu, J.-P., and Deline, P.: Multitemporal glacier inventory of the French Alps from the late 1960s
721 to the late 2000s, *Glob. Planet. Change*, 120, 24–37, <https://doi.org/10.1016/j.gloplacha.2014.05.004>, 2014.
- 722 Gruber, S. and Haeblerli, W.: Permafrost in steep bedrock slopes and its temperatures-related destabilization following climate
723 change, *J. Geophys. Res. Earth Surf.*, 112, 1–10, <https://doi.org/10.1029/2006JF000547>, 2007.
- 724 Gruber, S., Hoelzle, M., and Haeblerli, W.: Rock-wall temperatures in the Alps: Modelling their topographic distribution and
725 regional differences, *Permafrost Periglac. Process.*, 15, 299–307, <https://doi.org/10.1002/ppp.501>, 2004.
- 726 Guillet, G., Ravel, L., Beutel, J., and Deline, P.: Fracture kinematics in steep bedrock permafrost, Aiguille du Midi (3842 m
727 a.s.l., Chamonix Mont-Blanc, France), <https://doi.org/10.3929/ETHZ-B-000309262>, 2018.
- 728 Hales, T. C. and Roering, J. J.: Climatic controls on frost cracking and implications for the evolution of bedrock landscapes,
729 *J. Geophys. Res.*, 112, F02033–F02033, <https://doi.org/10.1029/2006JF000616>, 2007.

- 730 Hallet, B., Walder, J. S., and Stubbs, C. W.: Weathering by segregation ice growth in microcracks at sustained subzero
731 temperatures: Verification from an experimental study using acoustic emissions, *Permafr. Periglac. Process.*, 2, 283–300,
732 <https://doi.org/10.1002/ppp.3430020404>, 1991.
- 733 Hanson, S. and Hoelzle, M.: The thermal regime of the active layer at the Murtèl rock glacier based on data from 2002, *Permafr.*
734 *Periglac. Process.*, 15, 273–282, <https://doi.org/10.1002/ppp.499>, 2004.
- 735 Hasler, A., Gruber, S., Font, M., and Dubois, A.: Advective heat transport in frozen rock clefts: Conceptual model, laboratory
736 experiments and numerical simulation, *Permafr. Periglac. Process.*, 22, 378–389, <https://doi.org/10.1002/ppp.737>, 2011.
- 737 Hasler, A., Gruber, S., and Beutel, J.: Kinematics of steep bedrock permafrost, *J. Geophys. Res. Earth Surf.*, 117,
738 2011JF001981, <https://doi.org/10.1029/2011JF001981>, 2012.
- 739 Herms, I., Jódar, J., Soler, A., Vadillo, I., Lambán, L. J., Martos-Rosillo, S., Núñez, J. A., Arnó, G., and Jorge, J.: Contribution
740 of isotopic research techniques to characterize high-mountain-Mediterranean karst aquifers: The Port del Comte (Eastern
741 Pyrenees) aquifer, *Sci. Total Environ.*, 656, 209–230, <https://doi.org/10.1016/j.scitotenv.2018.11.188>, 2019.
- 742 Huggel, C., Allen, S., Deline, P., Fischer, L., Noetzi, J., and Ravel, L.: Ice thawing, mountains falling—are alpine rock slope
743 failures increasing, *Geol. Today*, 28, 98–104, <https://doi.org/10.1111/j.1365-2451.2012.00836.x>, 2012.
- 744 Krakauer, N. Y. and Temimi, M.: Stream recession curves and storage variability in small watersheds, *Hydrol. Earth Syst.*
745 *Sci.*, 15, 2377–2389, <https://doi.org/10.5194/hess-15-2377-2011>, 2011.
- 746 Krautblatter, M., Huggel, C., Deline, P., and Hasler, A.: Research Perspectives on Unstable High-alpine Bedrock Permafrost:
747 Measurement, Modelling and Process Understanding, *Permafr. Periglac. Process.*, 23, 80–88, <https://doi.org/10.1002/ppp.740>,
748 2012.
- 749 Krautblatter, M., Funk, D., and Günzel, F. K.: Why permafrost rocks become unstable: A rock-ice-mechanical model in time
750 and space, *Earth Surf. Process. Landf.*, 38, 876–887, <https://doi.org/10.1002/esp.3374>, 2013.
- 751 Lauber, U. and Goldscheider, N.: Use of artificial and natural tracers to assess groundwater transit-time distribution and flow
752 systems in a high-alpine karst system (Wetterstein Mountains, Germany), *Hydrogeol. J.*, 22, 1807–1824,
753 <https://doi.org/10.1007/s10040-014-1173-6>, 2014.
- 754 Legay, A., Magnin, F., and Ravel, L.: Rock temperature prior to failure: Analysis of 209 rockfall events in the Mont Blanc
755 massif (Western European Alps), *Permafr. Periglac. Process.*, 32, 520–536, <https://doi.org/10.1002/ppp.2110>, 2021.
- 756 Lehning, M., Bartelt, P., Brown, B., Russi, T., Stöckli, U., and Zimmerli, M.: snowpack model calculations for avalanche
757 warning based upon a new network of weather and snow stations, *Cold Reg. Sci. Technol.*, 30, 145–157,
758 [https://doi.org/10.1016/S0165-232X\(99\)00022-1](https://doi.org/10.1016/S0165-232X(99)00022-1), 1999.
- 759 Leinauer, J., Jacobs, B., and Krautblatter, M.: High alpine geotechnical real time monitoring and early warning at a large
760 imminent rock slope failure (Hochvogel, GER/AUT), *IOP Conf. Ser. Earth Environ. Sci.*, 833, <https://doi.org/10.1088/1755-1315/833/1/012146>, 2021.
- 762 Li, N., Zhang, P., Chen, Y., and Swoboda, G.: Fatigue properties of cracked, saturated and frozen sandstone samples under
763 cyclic loading, *Int. J. Rock Mech. Min. Sci.*, 40, 145–150, [https://doi.org/10.1016/S1365-1609\(02\)00111-9](https://doi.org/10.1016/S1365-1609(02)00111-9), 2003.
- 764 Magnin, F. and Josnin, J.-Y.: Water Flows in Rockwall Permafrost : a Numerical Approach Coupling Hydrological and
765 Thermal Processes, *J. Geophys. Res. Earth Surf.*, 2021.

- 766 Magnin, F., Brenning, A., Bodin, X., Deline, P., and Ravel, L.: Modélisation statistique de la distribution du permafrost de
767 paroi : application au massif du Mont Blanc, *Géomorphologie Relief Process. Environ.*, 21, 145–162,
768 <https://doi.org/10.4000/geomorphologie.10965>, 2015a.
- 769 Magnin, F., Deline, P., Ravel, L., Noetzi, J., and Pogliotti, P.: Thermal characteristics of permafrost in the steep alpine rock
770 walls of the Aiguille du Midi (Mont Blanc Massif, 3842 m a.s.l.), *Cryosphere*, 9, 109–121, [https://doi.org/10.5194/tc-9-109-](https://doi.org/10.5194/tc-9-109-2015)
771 2015, 2015b.
- 772 Magnin, F., Ravel, L., Ben-Asher, M., Bock, J., Cathala, M., Duvillard, P.-A., Jean, P., Josnin, J.-Y., Kaushik, S., Revil, A.,
773 and Deline, P.: From Rockfall Observation to Operational Solutions: Nearly 20 years of Cryo-gravitational Hazard Studies in
774 Mont-Blanc Massif, *Rev. Géographie Alp.*, 111–2, <https://doi.org/10.4000/rga.11703>, 2023.
- 775 Magnin, F., Ravel, L., Bodin, X., Deline, P., Malet, E., Krysiacki, J., and Schoeneich, P.: Main results of permafrost
776 monitoring in the French Alps through the *PermaFrance* network over the period 2010–2022, *Permafr. Periglac. Process.*, 35,
777 3–23, <https://doi.org/10.1002/ppp.2209>, 2024.
- 778 Maillat, E. T.: *Essais d'hydraulique souterraine & fluviale*, A. Hermann, 1905.
- 779 Manning, A. H. and Caine, J. S.: Groundwater noble gas, age, and temperature signatures in an Alpine watershed: Valuable
780 tools in conceptual model development, *Water Resour. Res.*, 43, 2006WR005349, <https://doi.org/10.1029/2006WR005349>,
781 2007.
- 782 Marcer, M., Ringsø Nielsen, S., Ribeyre, C., Kummert, M., Duvillard, P., Schoeneich, P., Bodin, X., and Genuite, K.:
783 Investigating the slope failures at the Lou rock glacier front, French Alps, *Permafr. Periglac. Process.*, 31, 15–30,
784 <https://doi.org/10.1002/ppp.2035>, 2020.
- 785 Maréchal, J. C., Perrochet, P., and Tacher, L.: Long-term simulations of thermal and hydraulic characteristics in a mountain
786 massif: The Mont Blanc case study, French and Italian Alps, *Hydrogeol. J.*, 7, 341–354,
787 <https://doi.org/10.1007/s100400050207>, 1999.
- 788 Maréchal, J.-C.: *Les circulations d'eau dans les massifs cristallins alpins et leurs relations avec les ouvrages souterrains*, EPFL,
789 <https://doi.org/10.5075/epfl-thesis-1769>, 1998.
- 790 Matsuoka, N. and Murton, J.: Frost weathering: recent advances and future directions, *Permafr. Periglac. Process.*, 19, 195–
791 210, <https://doi.org/10.1002/ppp.620>, 2008.
- 792 Matsuoka, N. and Sakai, H.: Rockfall activity from an alpine cliff during thawing periods, *Geomorphology*, 28, 309–328,
793 [https://doi.org/10.1016/S0169-555X\(98\)00116-0](https://doi.org/10.1016/S0169-555X(98)00116-0), 1999.
- 794 Mellor, M.: Mechanical properties of rocks at low temperatures, in: 2nd International Conference on Permafrost, Yakutsk,
795 International Permafrost Association, 334–344, 1973.
- 796 Noetzi, J., Isaksen, K., Barnett, J., Christiansen, H. H., Delaloye, R., Etzelmüller, B., Farinotti, D., Gallemann, T., Guglielmin,
797 M., Hauck, C., Hilbich, C., Hoelzle, M., Lambiel, C., Magnin, F., Oliva, M., Paro, L., Pogliotti, P., Riedl, C., Schoeneich, P.,
798 Valt, M., Vieli, A., and Phillips, M.: Enhanced warming of European mountain permafrost in the early 21st century, *Nat.*
799 *Commun.*, 15, 10508, <https://doi.org/10.1038/s41467-024-54831-9>, 2024.
- 800 [Pearson, K.: Notes on regression and inheritance in the case of two parents, *Biometrika*, 13, 25–45,](https://doi.org/10.1093/biomet/13.1.25)
801 <https://doi.org/10.1093/biomet/13.1.25>, 1920.

- 802 Pellet, C. and Hauck, C.: Monitoring soil moisture from middle to high elevation in Switzerland: set-up and first results from
803 the SOMOMOUNT network, *Hydrol. Earth Syst. Sci.*, 21, 3199–3220, <https://doi.org/10.5194/hess-21-3199-2017>, 2017.
- 804 Phillips, M., Haberkorn, A., Draebing, D., Krautblatter, M., Rhyner, H., and Kenner, R.: Seasonally intermittent water flow
805 through deep fractures in an Alpine Rock Ridge: Gemsstock, Central Swiss Alps, *Cold Reg. Sci. Technol.*, 125, 117–127,
806 <https://doi.org/10.1016/j.coldregions.2016.02.010>, 2016.
- 807 Ravel, L. and Deline, P.: Climate influence on rockfalls in high-alpine steep rockwalls: The north side of the aiguilles de
808 chamonix (mont blanc massif) since the end of the “Little Ice Age,” *Holocene*, 21, 357–365,
809 <https://doi.org/10.1177/0959683610374887>, 2011.
- 810 Ravel, L. and Deline, P.: A network of observers in the Mont-Blanc massif to study rockfall from high Alpine rockwalls,
811 *Geogr. Fis. E Din. Quat.*, 151–158, <https://doi.org/10.4461/GFDQ.2013.36.12>, 2013.
- 812 Ravel, L., Magnin, F., and Deline, P.: Impacts of the 2003 and 2015 summer heatwaves on permafrost-affected rock-walls
813 in the Mont Blanc massif, *Sci. Total Environ.*, 609, 132–143, <https://doi.org/10.1016/j.scitotenv.2017.07.055>, 2017.
- 814 Scandroglio, R., Stoll, V., and Krautblatter, M.: The driving force of all nature. Modelling water pressure and its stability
815 consequences on alpine bedrock slopes, *IOP Conf. Ser. Earth Environ. Sci.*, 833, <https://doi.org/10.1088/1755-1315/833/1/012109>, 2021.
- 817 Scandroglio, R., Weber, S., Rehm, T., and Krautblatter, M.: Decadal in situ hydrological observations and empirical modeling
818 of pressure head in a high-alpine, fractured calcareous rock slope, *Earth Surf. Dyn.*, 13, 295–314, <https://doi.org/10.5194/esurf-13-295-2025>, 2025.
- 820 Scherler, M., Hauck, C., Hoelzle, M., Stähli, M., and Völksch, I.: Meltwater infiltration into the frozen active layer at an alpine
821 permafrost site, *Permafr. Periglac. Process.*, 21, 325–334, <https://doi.org/10.1002/ppp.694>, 2010.
- 822 Smith, R. E. (Ed.): *Infiltration theory for hydrologic applications*, American Geophysical Union, Washington, DC, 1 pp.,
823 <https://doi.org/10.1029/WM015>, 2002.
- 824 Staub, B. and Delaloye, R.: Using Near-Surface Ground Temperature Data to Derive Snow Insulation and Melt Indices for
825 Mountain Permafrost Applications: Snow and Melt Indices Derived from GST Data, *Permafr. Periglac. Process.*, 28, 237–248,
826 <https://doi.org/10.1002/ppp.1890>, 2017.
- 827 Strauhal, T., Loew, S., Holzmann, M., and Zangerl, C.: Detailed hydrogeological analysis of a deep-seated rockslide at the
828 Gepatsch reservoir (Klasgarten, Austria), *Hydrogeol. J.*, 24, 349–371, <https://doi.org/10.1007/s10040-015-1341-3>, 2016.
- 829 Su, G. W., Geller, J. T., Pruess, K., and Hunt, J.: Overview of preferential flow in unsaturated fractures, *Geophys. Monogr. Ser.*,
830 122, 147–155, <https://doi.org/10.1029/GM122p0147>, 2000.
- 831 Sun, Z., Ma, R., Wang, Y., Ma, T., and Liu, Y.: Using isotopic, hydrogeochemical-tracer and temperature data to characterize
832 recharge and flow paths in a complex karst groundwater flow system in northern China, *Hydrogeol. J.*, 24, 1393–1412,
833 <https://doi.org/10.1007/s10040-016-1390-2>, 2016.
- 834 Tallaksen, L. M.: A review of baseflow recession analysis, *J. Hydrol.*, 165, 349–370, [https://doi.org/10.1016/0022-1694\(94\)02540-R](https://doi.org/10.1016/0022-1694(94)02540-R), 1995.

- 836 Thompson, S. S., Kulesa, B., Essery, R. L. H., and Lüthi, M. P.: Bulk meltwater flow and liquid water content of snowpacks
837 mapped using the electrical self-potential (SP) method, *The Cryosphere*, 10, 433–444, <https://doi.org/10.5194/tc-10-433-2016>,
838 2016.
- 839 Tsang, C.-F., Tsang, Y. W., Birkhölzer, J., and Moreno, L.: Dynamic Channeling of Flow and Transport in Saturated and
840 Unsaturated Heterogeneous Media, in: *Geophysical Monograph Series*, edited by: Evans, D. D., Nicholson, T. J., and
841 Rasmussen, T. C., American Geophysical Union, Washington, D. C., 33–44, <https://doi.org/10.1029/GM042p0033>, 2013.
- 842 Vionnet, V., Brun, E., Morin, S., Boone, A., Faroux, S., Le Moigne, P., Martin, E., and Willemet, J.-M.: The detailed snowpack
843 scheme Crocus and its implementation in SURFEX v7.2, *Geosci. Model Dev.*, 5, 773–791, [https://doi.org/10.5194/gmd-5-](https://doi.org/10.5194/gmd-5-773-2012)
844 [773-2012](https://doi.org/10.5194/gmd-5-773-2012), 2012.
- 845 Walter, F., Amann, F., Kos, A., Kenner, R., Phillips, M., de Preux, A., Huss, M., Tognacca, C., Clinton, J., Diehl, T., and
846 Bonanomi, Y.: Direct observations of a three million cubic meter rock-slope collapse with almost immediate initiation of
847 ensuing debris flows, *Geomorphology*, 351, 106933–106933, <https://doi.org/10.1016/j.geomorph.2019.106933>, 2020.
- 848 Weber, S., Beutel, J., Faillettaz, J., Hasler, A., Krautblatter, M., and Vieli, A.: Quantifying irreversible movement in steep,
849 fractured bedrock permafrost on Matterhorn (CH), *Cryosphere*, 11, 567–583, <https://doi.org/10.5194/tc-11-567-2017>, 2017.

850